J. Fluid Mech. (2009), *vol.* 623, *pp.* 121–148.
doi:10.1017/S002211200800503X Printed in the United Kingdom

Revisiting the aerodynamics of hovering flight using simple models

CHENG-TA HSIEH[1,2], CHIEN C. CHANG[1,2,†] AND CHIN-CHOU CHU[1,†]

[1]Institute of Applied Mechanics and Taida Institute of Mathematical Sciences, National Taiwan University, Taipei 106, Taiwan, ROC

[2]Division of Mechanics, Research Center for Applied Sciences, Academia Sinica, Taipei 115, Taiwan, ROC

(Received 25 March 2008 and in revised form 20 November 2008)

In this study, we revisit two simplified models of hovering motion for fruit fly and dragonfly from the perspective of force decomposition. The unsteady aerodynamics are analysed by examining the lift force and its four constituent components, each of which is directly related to a physical effect. These force components include one from the vorticity within the flow, one from the surface vorticity and two contributions credited to the motion of the insect wing. According to the phase difference in the models, a hovering motion can be classified into one of three types: symmetric, advanced and delayed rotations. The relative importance of the force components under various flow conditions are carefully analysed. It is shown that the symmetric rotation has the maximum vorticity lift (from volume and surface vorticity), but the optimal average lift is attained for an advanced rotation, which, compared to the symmetric rotation, increases the force contribution due to the unsteady surface motion at the expense of sacrificing contribution from the vorticity. By identifying the variations of the vorticity lift with flow characteristics, we may further explore the detailed mechanisms associated with the unsteady aerodynamics at different phases of hovering motion. For the different types of rotation, the insect wing shares the same mechanism of gaining lift when in the phase of driving with a fuller speed but exhibits different mechanisms at turning from one phase of motion to another. Moreover, we also examine the effects of the Reynolds number in an appropriate range and evaluate the performance of different wing profiles from symmetric to largely cambered.

1. Introduction

Insect flight has been of great interest to general audience, not only to scientists and biologists. For example, consider the hovering motion. Ellington (1984) showed that the classical lifting line theory quasi-steady assumption failed in explaining how an insect supports itself and considered that the lift supporting the insect comes from the unsteadiness. In view of advances of numerical and measurement techniques in late years, various studies of unsteady aerodynamics that have helped comprehend lift generation of insect flight have been concluded.

Weis-Fogh (1973) proposed the clap-and-fling mechanism by observing the wasp *Encarsia formosa*, and Lighthill (1973) presented a detailed theory for the mechanism.

† Email address for correspondence: mechang@gate.sinica.edu.tw; chucc@iam.ntu.edu.tw

The leading-edge vortex (LEV) produced on the model of fling what is termed delayed stall, which Maxworthy (1979) credited to be an important source of the lift. Ellington *et al.* (1996) observed the hawkmoth *Manduca sexta* and found the LEV attached on the wings could be important for insect flight. It was also confirmed by Dickinson & Götz (1993) and Dickinson (1994). Dickinson, Lehmann & Sane (1999) measured the aerodynamic forces from the dynamically scaled model of the fruit fly wing and concluded that the generation of enhanced lift of insects comes from the delayed stall during the translation of the stroke, rotational circulation and wake capture at the beginning and near the end of the stoke. It was also shown that the kinematics of flapping wing have an effect on the forces of the LEV (Wang 2000*b*; Sane & Dickinson 2001, 2002). Srygley & Thomas (2002) trained butterflies to fly freely and captured the images of the air flow around their wings. They concluded that butterflies use a variety of unconventional aerodynamic mechanisms to generate force. In addition, other factors, such as geometric cross-section, kinematic models and Reynolds number, have effects on the applied forces and unsteady flow phenomena of insect flight by experiments and numerical computations. Smith, Wilkin & Williams (1996) showed the advantages of an unsteady panel method in modelling the aerodynamic forces on rigid flapping wings. Wang (2000*a*) studied the two-dimensional vortex dynamics for insect hovering and examined the effects of the Reynolds number on the averaged lift. Sun & Tang (2002) compared the experimental results of Dickinson *et al.* (1999) with their numerical calculations and suggested that the force peaks that occur at the beginning of the half-stroke were due to the rapid acceleration of the wing. Ramamurti & Sandberg (2002) performed a three-dimensional computational study of the aerodynamics of insect flight with particular emphasis on the effect of phasing between the translational and rotational motions. Isogai *et al.* (2004) simulated three-dimensional unsteady viscous flow of dragonfly hovering and were mainly concerned with the total lift force and specified necessary power for the motion. Bos *et al.* (2008) compared four two-dimensional models for fruit flies, all scaled at the Reynolds number $Re = 110$, and showed significant difference in forces from the simplified wing kinematic models.

Although two-dimensional flow patterns are less realistic for insect flight, they still enable us to identify some essential features based on the following reasons: Two-dimensional geometry is simple and gives good approximation for the wing with high aspect ratio. Wang, Birch & Dickinson (2004) concluded that two-dimensional unsteady forces turn out to approximate well three-dimensional experiment for insect flight. In addition, it might be sufficient to explain high-lift mechanisms of the hovering motion. In spite of these important works, there still exit puzzling and unsatisfactory explanations about the high-lift mechanisms of the hovering motion even for two-dimensional flow. In particular, Sane (2003) showed that the cause of this discrepancy between the numerical simulations (Sun & Tang 2002) and the particle image velocimetric observations (Dickinson *et al.* 1999) remains unclear. Wang (2005) remarked that both the acceleration and wing–wake interaction must have an effect on the forces. However, these effects have eluded simple quantitative prediction, thus making it difficult to estimate their relative strengths. Lehmann (2008) mentioned that apart from this controversial view on the wake capture mechanism, it remains unclear how exactly the benefit of wake capture changes during fast forward or manoeuvring flight of an insect when the wings experience additional fluid components produced by the animal's own body motion. It has been clear that the high lift of hovering flight cannot be explained by steady aerodynamics but comes from the unsteadiness of the motion. But the term unsteadiness is unclear because it may refer to the wing

with unsteady rotation and acceleration and the unsteady contributions from within the flow region or on the body surface.

In the literature, there are several useful force theories which shed light on different aspects of hydrodynamic or aerodynamic forces. The circulation theory was the earliest used to predict the lift (see, e.g., Howarth 1935). Weis-Fogh (1973) predicted the lift coefficient of dragonfly hovering based on the blade element theory. Rayner (1979) and Ellington (1984) employed the flow momentum balance in the study of helicopters to determine the force in flapping flight. Wu (1981) provided some relationships between forces and the rate of change of vorticity moments in the viscous flow. Lighthill (1979, 1986) developed the ideas which validate a separation of hydrodynamic loadings into potential flow forces and vortex flow forces. The applied force was deliberately explained as the rate of change of a momentum, defined by an absolutely convergent integral. In general, experimental works report measured forces on a wing by force sensor, and numerical computed results give forces by integrating the stress over the wing surface. It is now unsteadiness that has been recognized as the cause of the lift of an insect in hovering motion. But it is difficult to solely identify the vortex wake with the generation of high lift, as there are other unsteady contributions to the lift in the hovering motion. As a matter of fact, the term 'unsteadiness' includes the time-varying motion of the wing and time-varying flow within the fluid as well as the time-varying surface vorticity on the wing surface.

Some time ago, Chang (1992) proposed a diagnostic force theory for real viscous flow to separate potential forces such as added mass and inertial forces and to distinguish the contributions of individual fluid elements to aerodynamic forces. The theory starts from the D'Alembert theorem that the incompressible potential flow predicts no force will be exerted on a body if the incident flow is a constant uniform stream. It is noteworthy that incompressible potential flow means that there is no single fluid element possessing non-zero vorticity or dilation. It is therefore considered that in a more realistic flow, any fluid element with non-zero vorticity or dilation may be considered a source of the hydrodynamic force. Based on this observation, Chang (1992) proposed to decompose the force in any given direction into three components: (i) the potential force due to the body motion or the accelerating incident stream; (ii) the force due to vorticity strictly within the flow region; (iii) the force due to the surface vorticity, which can further be divided to two parts – one is the frictional force, and the other is called the friction-like force. Each of (ii) and (iii) is written in the form of an integral in which the integrands are appropriately called the volume and surface force elements, respectively. It is notable that the volume element rapidly decays away from the body and accounts for most force contribution for largely separated flow. The viewpoint has found some applications (e.g., Chu *et al.* 1996), and was extended to compressible flow to examine force contributions by various structures in the flow (Chang & Lei 1996*a*, *b*). More directly related to the present interest are the works of Howe (1989, 1995) in which the author presented the force decomposition with great clarity and applied it to bubbles, droplets and bodies at low and high Reynolds numbers. The method of analysis was also later applied to analyse lift and drag fluctuations of a sphere (Howe, Lauchle & Wang 2001). In a recent paper, Biesheuvel & Hagmeijer (2006) presented the early idea by Burgers (1920) in terms of the vorticity distribution and pointed at the close relationship of Burgers's formula with those of Lighthill (1979, 1986). The authors went further to establish the connection between these earlier formulas and the more recent work on aerodynamic forces by Kambe (1986) and Howe (1989, 1995). The force decomposition was recently extended

to flow about many bodies with applications to bubble dynamics (Ragazzo & Tabak 2007) and for force diagnosis (Chang, Yang & Chu 2008).

In the present study, the viewpoint with force decomposition is used to examine the hovering flights of the fruit fly and dragonfly in their respective simplified two-dimensional models (Dickinson *et al.* 1999; Wang 2000*a*; Wang *et al.* 2004) and illustrate how the theory of force decomposition sheds further light on several contributions from unsteadiness to the lift generated at various stages of hovering flight and their dependence on the type of motion, wing profile and Reynolds number as well as the location of the axis of rotation.

2. Auxiliary potential

In order to analyse various force contributions to the flow about a finite body, we need to introduce auxiliary potential functions. Let us first determine the nature of potential solution. The potential solution ϕ satisfies $\nabla^2\phi = 0$ and is required to vanish at infinity at which the fluid is at rest. The general solution at great distances r from the body in two dimensions is given by

$$\phi = -(\boldsymbol{A}\cdot\nabla)\log r + \cdots = -\frac{\boldsymbol{A}\cdot\hat{\boldsymbol{r}}}{r} + \cdots, \tag{2.1}$$

where $\hat{\boldsymbol{r}}$ is the unit vector along the direction of $\boldsymbol{r}$. In (2.1), the vector $\boldsymbol{A}$ depends on the actual shape and the motion of the wing and is independent of the coordinates. The exact $\boldsymbol{A}$ requires a complete solution of the equation $\nabla^2\phi = 0$ (cf. Landau & Lifshitz 1987) and appropriate boundary conditions. It should be kept in mind that the corresponding velocity $\nabla\phi$ decays like $1/r^2$ in two dimensions. A similar formula holds in three dimensions. The boundary conditions will be specified depending on which force direction is considered. If $\boldsymbol{s}$ is the unit vector along the force direction of interest, then we require $\boldsymbol{n}\cdot\nabla\phi = -\boldsymbol{n}\cdot\boldsymbol{s}$ on the body surface. The potential function that satisfies this condition is used to decompose the pressure force along the $\boldsymbol{s}$ direction for real viscous fluid to added-mass force, surface vorticity force and volume vorticity force as well as other possible contributions.

3. The force decomposition

Consider a single insect wing motion in air as shown in figure 1. Let ρ^* be the air density, μ^* the air viscosity, c^* the chord length of wing and U^*_{max} the maximum velocity. Take $c^*/2$ to be the reference length, $c^*/2U^*_{max}$ to be the reference time and $1/2\rho^* c^* U^{*2}_{max}$ to be the reference pressure. The flow field of the hovering motion is assumed to be governed by the Navier–Stokes equations and incompressibility condition which, in dimensionless form are given by

$$\frac{\partial \boldsymbol{v}}{\partial t} + (\boldsymbol{v}\cdot\nabla)\boldsymbol{v} = -\nabla p + \frac{2}{Re}\Delta\boldsymbol{v}; \tag{3.1}$$

$$\nabla\cdot\boldsymbol{v} = 0. \tag{3.2}$$

where p is the pressure; $\boldsymbol{v}$ is the velocity; and $Re = \rho^* c^* U^*_{max}/\mu^*$ is the Reynolds number. The most well-known formula for calculating the lift is

$$C_L = \int_S p\boldsymbol{n}\cdot\boldsymbol{j}\,\mathrm{d}A + \frac{2}{Re}\int_S \boldsymbol{n}\times\boldsymbol{\omega}\cdot\boldsymbol{j}\,\mathrm{d}A, \tag{3.3}$$

where $\boldsymbol{j}$ is the unit vector in the lift direction; $\boldsymbol{n}$ is the inward normal to the wing surface; and $\boldsymbol{\omega}$ denotes the vorticity. Now we show how to gain the formula of force

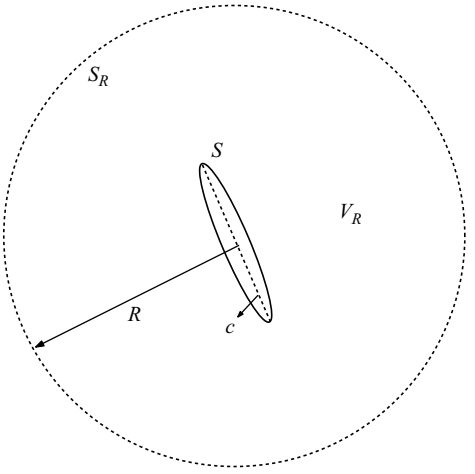

FIGURE 1. Schematic of the wing: c is the chord length; S is the wing surface; and V_R is the volume enclosed by the wing surface S and a large surface S_R of radius R. All the quantities are dimensionless.

decomposition. First of all, we are concerned with the lift direction. Let ϕ satisfy the boundary condition $\boldsymbol{n}\cdot\nabla\phi = -\boldsymbol{n}\cdot\boldsymbol{j}$ (i.e. $\boldsymbol{s}=\boldsymbol{j}$), which is the unit velocity on the body. Let V_R be the volume of fluid enclosed by a cylindrical surface S_R of large radius R and the wing surface S. Equation (3.1) can be written

$$-\nabla p = \frac{\partial \boldsymbol{v}}{\partial t} + \frac{1}{2}\nabla|\boldsymbol{v}|^2 - \boldsymbol{v}\times\boldsymbol{\omega} + \frac{2}{Re}\nabla\times\boldsymbol{\omega}. \tag{3.4}$$

Here we will use the two identities $\boldsymbol{v}\cdot\nabla\phi = \nabla\cdot(\boldsymbol{v}\phi)$ and $(\nabla\times\boldsymbol{\omega})\cdot\nabla\phi = \nabla\cdot(\boldsymbol{\omega}\times\nabla\phi)$ and apply the divergence theorem. Taking inner products with $\nabla\phi$ on both sides of (3.4) and integrating within the flow region V_R yields

$$\begin{aligned}-\int_{S\cup S_R} p\boldsymbol{n}\cdot\nabla\phi\,\mathrm{dA} = &\int_{S\cup S_R}\phi\frac{\partial\boldsymbol{v}}{\partial t}\cdot\boldsymbol{n}\,\mathrm{d}A + \frac{1}{2}\int_{S\cup S_R}|\boldsymbol{v}|^2\nabla\phi\cdot\boldsymbol{n}\,\mathrm{d}A\\ &-\int_{V_R}\boldsymbol{v}\times\boldsymbol{\omega}\cdot\nabla\phi\,\mathrm{d}V + \frac{2}{Re}\int_{S\cup S_R}\boldsymbol{n}\times\boldsymbol{\omega}\cdot\nabla\phi\,\mathrm{d}A.\end{aligned} \tag{3.5}$$

The fluid is at rest in the far field from the body. Applying this boundary condition and noting that $\nabla\phi$ decays like $1/r^2$, we can carry out the integral on the left-hand side and the first, second and fourth ones on the right-hand side with $R\to\infty$ and $V_R\to V$ (entire fluid region) to obtain

$$\begin{aligned}-\int_S p\boldsymbol{n}\cdot\nabla\phi\,\mathrm{d}A = &\int_S\phi\frac{\partial\boldsymbol{v}}{\partial t}\cdot\boldsymbol{n}\,\mathrm{d}A + \frac{1}{2}\int_S|\boldsymbol{v}|^2\nabla\phi\cdot\boldsymbol{n}\,\mathrm{d}A\\ &-\int_V\boldsymbol{v}\times\boldsymbol{\omega}\cdot\nabla\phi\,\mathrm{d}V + \frac{2}{Re}\int_S\boldsymbol{n}\times\boldsymbol{\omega}\cdot\nabla\phi\,\mathrm{d}A.\end{aligned} \tag{3.6}$$

Recall the boundary condition $\boldsymbol{n}\cdot\nabla\phi = -\boldsymbol{n}\cdot\boldsymbol{j}$ on the body surface for the left-hand side; this gives $-\int_S p\boldsymbol{n}\cdot\nabla\phi\,\mathrm{d}A = \int_S p\boldsymbol{n}\cdot\boldsymbol{j}\,\mathrm{d}A$. Finally if the frictional force $(2/Re)\int_S\boldsymbol{n}\times\boldsymbol{\omega}\cdot\boldsymbol{j}\,\mathrm{d}A$ (i.e. the second term on the right-hand side of (3.3)) is included, the complete decomposition for the lift force can be obtained:

$$C_L = C_{La} + C_{Lm} + C_{Lv} + C_{Ls}, \tag{3.7}$$

where

$$\left.\begin{aligned} C_{La} &= \int_S \phi \frac{\partial \boldsymbol{v}}{\partial t} \cdot \boldsymbol{n}\, \mathrm{d}A; \qquad C_{Lm} = \frac{1}{2}\int_S |\boldsymbol{v}|^2 \nabla\phi \cdot \boldsymbol{n}\, \mathrm{d}A; \\ C_{Lv} &= -\int_V \boldsymbol{v} \times \boldsymbol{\omega} \cdot \nabla\phi\, \mathrm{d}V; \; C_{Ls} = \frac{2}{\mathrm{Re}}\int_S \boldsymbol{n} \times \boldsymbol{\omega} \cdot (\nabla\phi + \boldsymbol{j})\, \mathrm{d}A. \end{aligned}\right\} \tag{3.8}$$

In (3.8), C_{La} is the contribution associated with the acceleration of the wing; C_{Lm} corresponds to the contribution by the velocity of the wing; C_{Ls} denotes the contribution by the surface vorticity and friction on the wing surface; and C_{Lv} represents the contribution of pressure force due to vorticity within the flow field. In particular, the integrand $-\boldsymbol{v} \times \boldsymbol{\omega} \cdot \nabla\phi$ is called the volume lift element, and $(2/Re)\boldsymbol{n} \times \boldsymbol{\omega} \cdot (\nabla\phi + \boldsymbol{j})$ is called the surface lift element, where the part with $\nabla\phi$ is called the friction-like force. Either of them may be termed the vortex force elements. A salient feature is only the volume lift elements near the body contribute significantly to the lift force because $\nabla\phi$ is rapidly decaying away from the body. Also the potential function ϕ can be considered the geometric factor, for each flow condition can be associated with a unique ϕ. It is noted that among the force components, C_{La} and C_{Lm} are determined by the boundary conditions and the geometric profile, while the determination of C_{Lv} and C_{Ls} requires solution of the fluid flow.

Note that if we consider the force in drag direction, say $\boldsymbol{s} = \boldsymbol{i}$, then ϕ has to satisfy $\boldsymbol{n} \cdot \nabla\phi = -\boldsymbol{n} \cdot \boldsymbol{i}$ on the wing surface. The force along the $\boldsymbol{i}$ direction is decomposed by

$$C_D = C_{Da} + C_{Dm} + C_{Dv} + C_{Ds}. \tag{3.9}$$

Here, the numerical results are obtained by using the deterministic vortex method (Chang & Chern 1991) and the SimpleC method of the commercial code FLUENT based on the control-volume method. Moreover, a conformal hybrid grid is used in the numerical method. In each time interval, the grid deformation is adjusted by the path of the wing to achieve numerical stability, according to the method of spring analogy and remeshing, and governed by the geometric conservation law (GCL; see, e.g., Thomas & Lombard 1979). In the present study, the total lift coefficient C_L is obtained by summing up all the lift components C_{Lm}, C_{La}, C_{Lv} and C_{Ls}. To ensure its accuracy, C_L will also be computed according to (3.3), and the computed result is denoted by $C_L(p)$.

4. Results and discussion

In this section, we are concerned with the simplified models for fruit fly and dragonfly, respectively. The two models basically exhibit different mechanisms in generating unsteady lifts but also share some common features as we vary the phase difference in the models. It is also interesting to study the effects of the Reynolds number in an appropriate range for insect flight and evaluate the performance of different wing profiles on the total lift and the contributing components.

4.1. *Model for fruit fly motion*

The motion for fruit fly is performed with $A_0^*/c^* = 4.8$ and $f^* = 0.25$ Hz. The Reynolds number Re is 115. The motion of the elliptic wing with aspect ratio 8 is given by $A(t) = A_0/2[\cos(2\pi f t) - 1]$. The rotation is about the middle chord of the wing, and the angle of attack is $\alpha(t) = \pi/2 + \pi/4[\sin(2\pi f t + \delta)]$ with $f = 1/T = c^* f^*/2U_{max}^*$. The rotation is set to be the advance if $(\delta > 0)$, symmetric if $(\delta = 0)$ and delayed if $(\delta < 0)$. In this study we consider seven values of δ, which include $\delta = -\pi/4$, $-3\pi/8$, $-\pi/2$

δ	$\alpha(0)$	$\bar{C}_L(p)$	$\bar{C}_L$	$\bar{C}_{Lm}$	$\bar{C}_{La}$	$\bar{C}_{Lv}$	$\bar{C}_{Ls}$
$\pi/2$	135°	0.275	0.274	−0.001	0.182	−0.0001	0.093
$3\pi/8$	131.57°	0.589	0.589	−0.001	0.169	0.252	0.169
$\pi/4$	121.82°	0.723	0.724	0.001	0.130	0.372	0.221
0	90°	0.543	0.547	0.002	0	0.361	0.184
$-\pi/4$	58.18°	0.260	0.263	0.002	−0.130	0.297	0.094
$-3\pi/8$	48.43°	0.109	0.112	0.001	−0.169	0.229	0.051
$-\pi/2$	45°	−0.271	−0.271	0.001	−0.182	0.003	−0.093

TABLE 1. Various time-averaged lift coefficients versus phase difference δ for fruit fly hovering.

(delayed); $\delta = 0$ (symmetric); $\delta = \pi/4$, $3\pi/8$, $\pi/2$ (advanced). The simulated motion is started from rest, and the lift reaches a stationary state after three strokes. Here we chose the sixth period for investigation.

4.1.1. *Influence of the phase difference between translation and rotation*

Table 1 presents a synoptic view of the distinctions of the three types of rotation by summarizing the lift components averaged over a time period. In this table, we have the maximum total lift $\bar{C}_L$ at $\delta = \pi/4$. In other words, the phase difference δ cannot be negative or significantly larger than $\delta = \pi/4$, as high lift is concerned. In all the motions, $\bar{C}_{Lm}$ is negligible compared to other components. Indeed, $\bar{C}_{La}$ increases with monotonously increasing phase angle δ from $\bar{C}_{La} = -0.182$ for $\delta = -\pi/2$ to $\bar{C}_{La} = 0.182$ for $\delta = \pi/2$. However, $\bar{C}_{Lv}$ and $\bar{C}_{Ls}$ favour the largest value at $\delta = \pi/4$. In the following discussion, we only consider the details for three values of δ, $-\pi/4$, 0 and $\pi/4$. The symmetric rotation is supported in full by the vortex lift ($\bar{C}_{Lv}+\bar{C}_{Ls}$), as $\bar{C}_{La}$ is zero and $\bar{C}_{Lm}$ is negligible. By switching from the symmetric rotation to the advanced, the most significant gain is the $\bar{C}_{La}$ coefficient (from 0 to 0.13), though there is also 8.81 % gain in the vortex lift (from 0.545 to 0.593). The increase in $\bar{C}_{Ls}$ (from 0.184 to 0.221) is 20.11 %, while the increase in $\bar{C}_{Lv}$ (from 0.361 to 0.373) is only 3.04 %. Nevertheless, the relative importance of the vortex lift for the advanced rotation which is 81.9 % ($(\bar{C}_{Lv}+\bar{C}_{Ls})/\bar{C}_L \times 100$ %) is still very significant. Compared to the symmetric rotation, the delayed rotation has a negative $\bar{C}_{La}(-0.130)$ and loses significantly the vortex lift by 28.3 % (from 0.545 to 0.391). It is also of interest to note that the surface vorticity is an important component of the vortex lift at these relatively low Reynolds number flows. If we consider the ratio $\bar{C}_{Ls}/(\bar{C}_{Lv}+\bar{C}_{Ls})$, it is 37.3 % for the advanced rotation and 33.8 % for the symmetric and drops to 24.0 % for the delayed.

In order to examine the unsteadiness, figures 2–4 show the time histories of the total lift C_L as well as the four lift components C_{La}, C_{Lm}, C_{Lv} and C_{Ls} for the three types of hovering flight in a period of motion. In all the types of motion, the insect wing is at its rightmost position in the beginning of the period. It is sufficient to study the behaviours of all the lift coefficients in a half period of time, say from $t/T = 0.25$ to $t/T = 0.75$. First, we note that C_{Lm} is uniformly small in all the three types of hovering flight. Then, the time history curve for C_{La} is almost entirely positive for the advanced rotation and half-positive and half-negative for the symmetric rotation, and then it is most of the time negative for the delayed rotation. Recall that C_{La} and C_{Lm} do not depend on the actual flow but are completely determined by the geometry and the specified motion of the insect wing. Hence, they are completely symmetric with respect to the rightward and leftward movements of the insect wing.

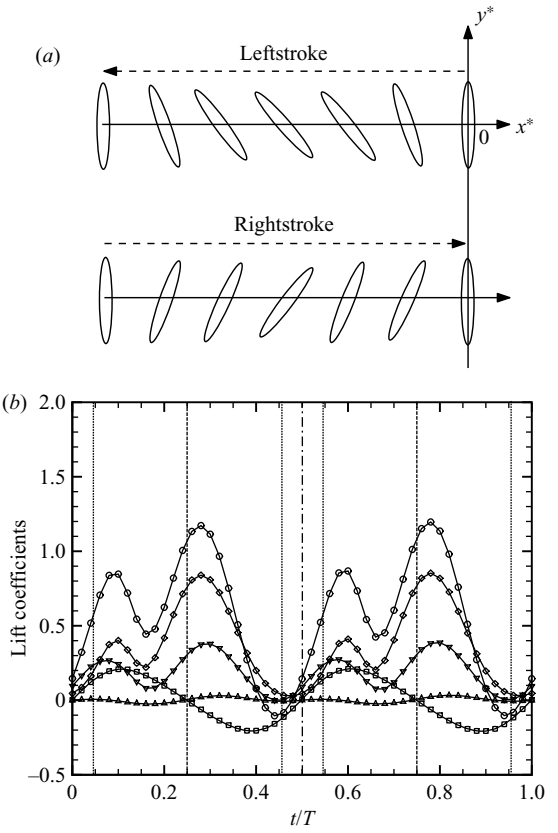

FIGURE 2. (*a*) Model 1 for the symmetric rotation with $\delta = 0$. (*b*) The time histories of the lift contribution. (○, C_L; △, C_{Lm}; □, C_{La}; ◇, C_{Lv}; ▽, C_{Ls}; vertical dash dots, $\alpha(t) = 90°$; vertical dots, the velocity is maximum and $\alpha(t) = 45°$ or 135°).

For the advanced rotation, the minimum ($=-0.07$) occurs when $t/T = 0.32$, while the maximum $C_{La}(=0.31)$ occurs when $t/T = 0.53$. For the symmetric rotation, the minimum ($=-0.21$) occurs when $t/T = 0.4$, while the maximum $C_{La}(=0.21)$ occurs when $t/T = 0.625$. For the delayed rotation, the minimum ($=-0.30$) occurs when $t/T = 0.47$, while the maximum $C_{La}(=0.07)$ occurs when $t/T = 0.69$. Next, we note that C_L, C_{Lv} and C_{Ls} for the advanced and symmetric rotations have very similar trends though differing somewhat in magnitude and temporal occasions. For each half period of time (from $t/T = 0.25$ to $t/T = 0.75$), we observe two maxima (one top and one local) and two minima (one bottom and one local) in the total lift C_L as well as in the volume vorticity and surface vorticity lift components C_{Lv} and C_{Ls}. Roughly speaking, the top maximum of $C_L(C_{Lv})$ occurs when the insect wing drives with full speed. The more interesting points are the local maximum and minimum appearing in the total lift C_L and the volume vortex lift C_{Lv} in the stage in which the insect wing manages turning from left to right. At the stage of turning, the translation speed of the insect wing becomes much lower than the full speed. For advanced rotation, a time behaviour is that C_{Lv} will soon get down to the bottom minimum -0.04 at $t/T = 0.42$, then rising to the local maximum 0.48 at $t/T = 0.58$ and then getting sucked down to the local minimum 0.16 at $t/T = 0.66$. It is noted that even at the moment in which C_{Lv} attains its negative bottom minimum, the insect wing maintains a positive total

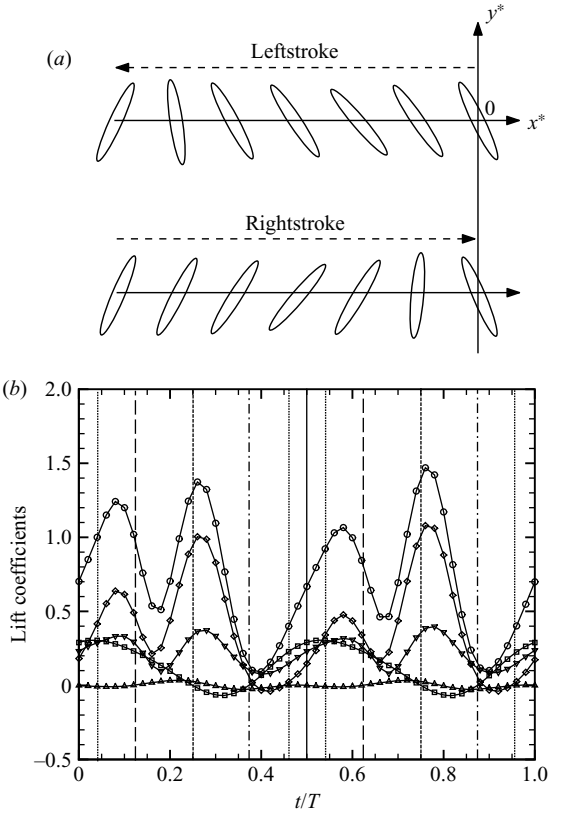

FIGURE 3. (*a*) Model 1 for the advanced rotation with $\delta = \pi/4$. (*b*) The time histories of the lift contribution. (○, C_L; △, C_{Lm}; □, C_{La}; ◇, C_{Lv}; ▽, C_{Ls}; vertical dash dots, $\alpha(t) = 90°$; vertical long dashes, $\alpha(t) = 45°$ or $135°$; vertical dots, the velocity is maximum).

lift C_L because of the positive contributions from $C_{Ls}(=0.08)$ and also $C_{La}(=0.1)$. The delayed rotation exhibits quite different behaviours. An obvious disadvantage is that C_{La} is negative most of the time. But the more profound difference is that there is neither a local maximum nor a local minimum in C_{Lv} (and C_L). At tuning, the delayed rotation has relatively small volume vortex lifts in contrast to other two types of motions, each of which has a significantly positive local maximum in the volume vortex lift C_{Lv}. These behaviours can be examined closely by exploring the distributions of the volume vortex lift elements at different times.

Figure 5(*a–f*) shows the snapshots of vorticity and vortex lift elements at six different instants during a time period for the advanced rotation. The sequence starts with the time instant ($t/T = 0.25$) at which the insect wing is in the middle of leftward motion. A useful remark is made here before we proceed with the details. In general, a region of vorticity of the same sign may contribute both positive and negative elements. Whether we have net positive or net negative force elements depends on the instant attitude of the insect wing and the actual flow conditions (Chang 1992). The insect wing drives with full speed in the middle of leftward movement ($t/T = 0.25$). The largest C_{Lv} is attained at $t/T = 0.27$ due to the net positive and intensive vortex lift elements which have been generated from the leading edge as well as from the trailing edge (figure 5*a*). Note that the angle made between the wing and the leftward

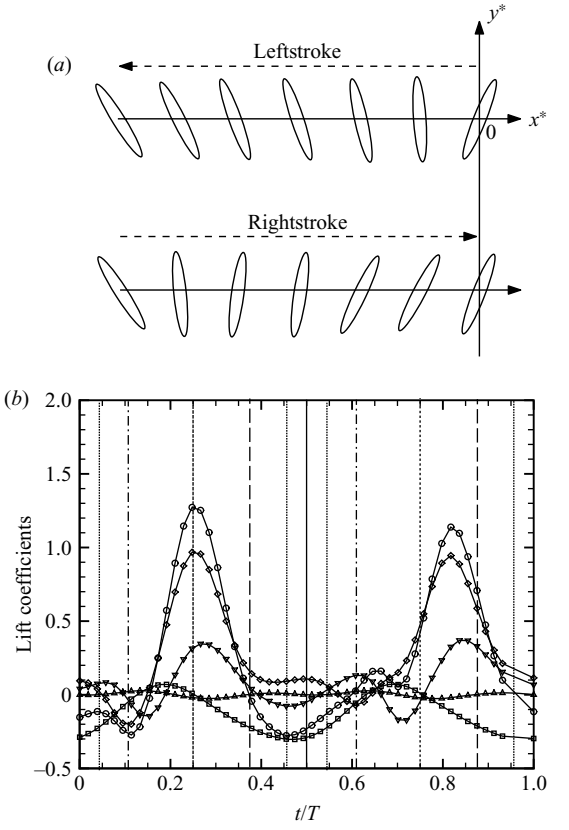

FIGURE 4. (*a*) Model 1 for the delayed rotation with $\delta = -\pi/4$. (*b*) The time histories of the lift contribution. (○, C_L; △, C_{Lm}; □, C_{La}; ◇, C_{Lv}; ▽, C_{Ls}; vertical dash dots, $\alpha(t) = 90°$; vertical long dashs, $\alpha(t) = 45°$ or 135°; vertical dots, the velocity is maximum).

direction is the high 62°, and thus the term of dynamic stall LEV is often used in this high volume vortex lift situation. As the insect wing is slowing down and preparing for turning, both the leading and trailing edges do not continue to generate intense vorticity. The insect wing experiences the smallest C_{Lv} at $t/T = 0.42$ when the wing makes the angle of 77° with the rightward direction (figure 5*b*). At this moment, the wing has turned from facing leftward to rightward but is still moving leftward. (The wing is at its leftmost position at $t/T = 0.5$). The LEV and trailing vortex are almost detached from the insect wing, and there are more negative vortex lift elements than the positive ones round the leading and trailing edges. These two vortices, which have been generated from the leading and trailing edges in the rear wake, are now turning to lie below the wing (or the front wake). Dickinson *et al.* (1999) called this behaviour 'wake capture', as the vortices are basically detached but are close enough to interact with the wing after turning. But the moment in which we observe wake capture does not necessarily imply a high vortex lift. Indeed, the two detached vortices of the wake capture, though differing in sign of vorticity, do contribute collaboratively to significantly positive lift elements. This mechanism that maintains vortex lift for the insect wing during turning is hereby called 'riding on lift elements', as the force contribution is concerned. However, these positive contributions are largely cancelled by the negative lift elements closely attached to the insect wing, yielding a slightly

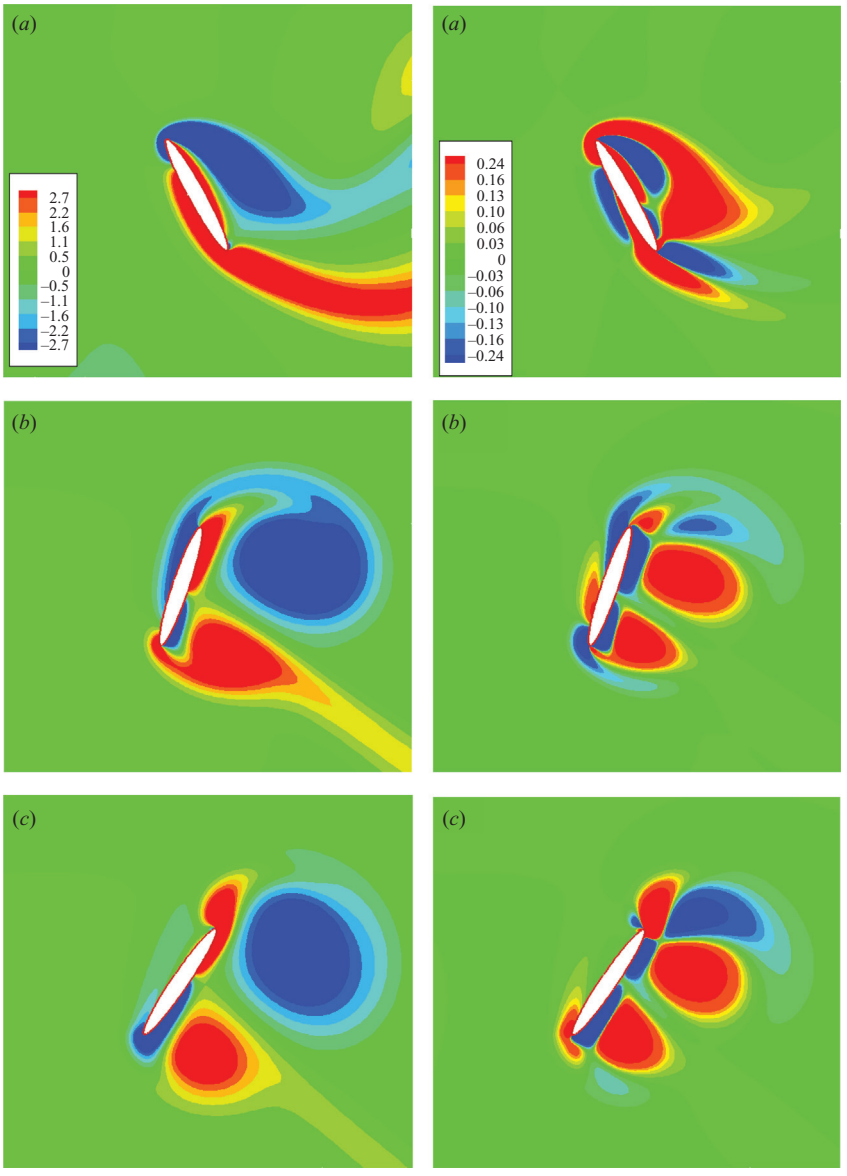

FIGURE 5. For legend see next page.

negative volume vortex lift $C_{Lv}(=-0.04)$. Nevertheless, it is very important that the flow pattern maintain wake capture or riding on lift elements for a while. For example, consider the time instant $t/T=0.5$. As the wing is further rotated at turning, new vorticity is generated from both the leading and trailing edges, contributing to positive lift elements (figure 5*c*). The vortex lift rises again. By time $t/T=0.58$, the insect wing moves rightward and makes the angle of 47°. While the wing is still effectively riding on lift element in the front wake, intense new vorticity has been generated from the leading and trailing edges, contributing net positive elements substantially (figure 5*d*). As a result, the insect wing at this moment benefits most from maintaining the mechanism of wake capture or riding on lift elements, gaining the local maximum

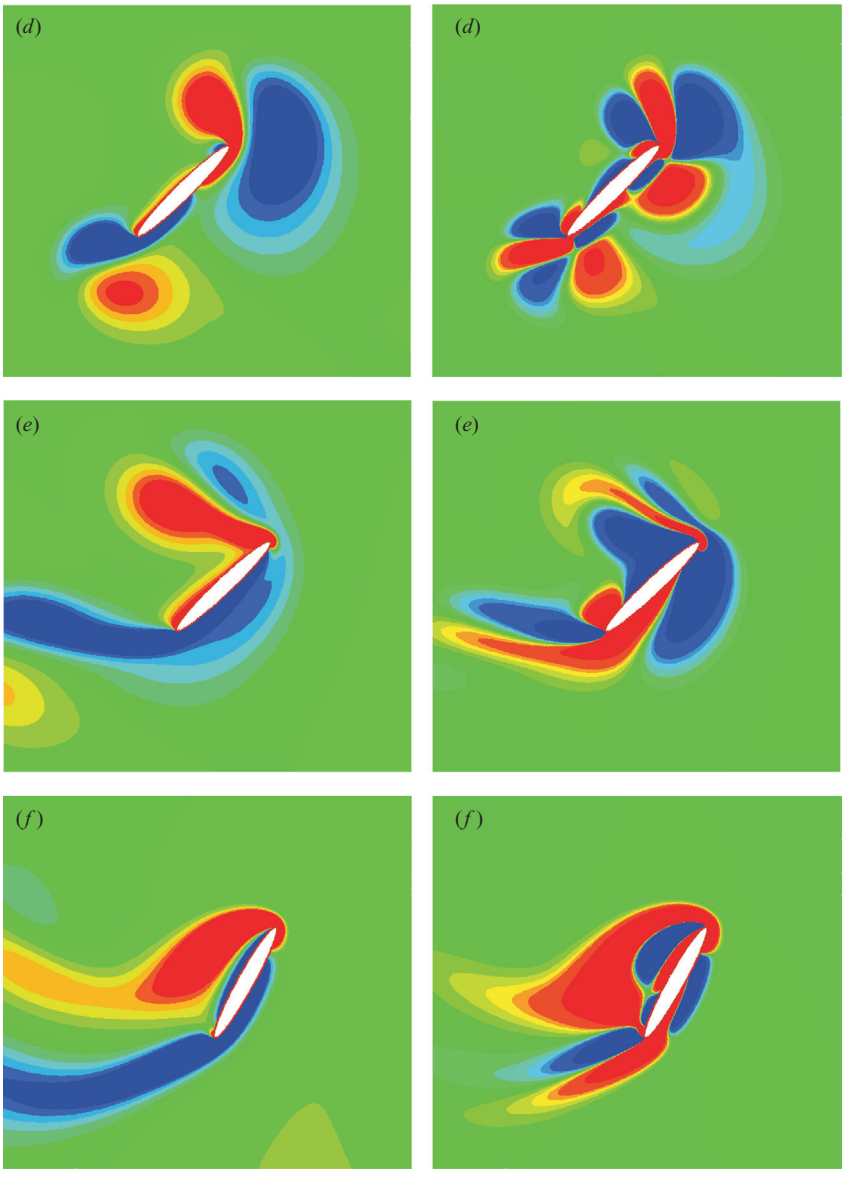

FIGURE 5. Selected plots of vorticity and lift elements for the advanced rotation with $\delta = \pi/4$. Left: vorticity contour (red, anticlockwise; blue, clockwise). Right: lift force element contour (red, positive lift elements; blue, negative lift elements). (*a*) $t/T = 0.27$, $\alpha(t) = 118°$, $v = -0.99$; (*b*) $t/T = 0.42$, $\alpha(t) = 77°$, $v = -0.48$; (*c*) $t/T = 0.50$, $\alpha(t) = 58°$, $v = 0$; (*d*) $t/T = 0.58$, $\alpha(t) = 47°$, $v = 0.48$; (*e*) $t/T = 0.66$, $\alpha(t) = 46°$, $v = 0.84$; (*f*) $t/T = 0.77$, $\alpha(t) = 62°$, $v = 0.99$; v is the translational velocity normalized by U_{max}.

in the volume vortex lift C_{Lv} (figure 5*d*). Now, when the wing slows its rotation, less vorticity is generated round the leading and trailing edges. As the wing moves further rightward, the two 'ridden-on' vortices in the front wake merge together to form a single region of positive lift elements near the trailing edge. At $t/T = 0.66$, the budget of positive and negative lift elements yields the local minimum (which is positive) in the vortex lift C_{Lv} (figure 5*e*). Then, as the insect drives again in full speed, the

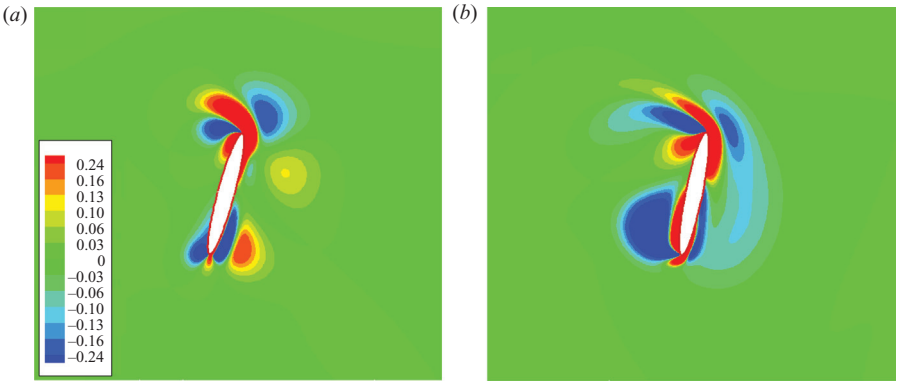

FIGURE 6. (*a*) Lift elements of the symmetric rotation at $t/T = 0.55$. (*b*) Lift elements of the delayed rotation at $t/T = 0.66$. (Red: positive lift elements; blue: negative lift elements.)

wing regains its maximum volume vortex lift soon after it is in the middle flight of rightward motion (figure 5*f*).

The most interesting behaviour associated with the advanced rotation is the mechanism of riding on lift elements of the previously detached vortices. As a comparison, figure 6(*a*, *b*) shows the snapshots of lift elements for the symmetric and delayed rotations when the wing makes an angle of about 77° in the rightward direction. This mechanism is less visible for the symmetric rotation and does not exist at all for the delayed rotation. For the symmetric rotation, the positive force elements are mainly generated from the leading edge and come less from the detached vortex near the trailing edge. For the delayed rotation, the positive force elements are mainly generated from both the leading and trailing edges.

If we look into the surface lift elements for advanced rotation, there are two distinguished distributions associated with the movement of the wing with a fuller speed or turning its direction of rotation. In either case, the lift elements are larger in magnitude at the leading edge than at the trailing edge, and in turn, the lift elements near both edges are much larger than at the rest of the wing surface. As the wing is moving with a fuller speed ($t/T = 0.28$) in figure 3, the lift elements on the front side are large and positive at the leading edge, become negative but small in the middle portion and then turn to be positive and mildly large at the trailing edge. The net C_{Ls} is 0.38. The lift elements on the rear side are large and positive at the leading edge, become small away from the leading edge and then turn to be mildly negative at the trailing edge. As the wing is turning its direction of rotation ($t/T = 0.4$), the lift elements are largely negative at the leading edge, separate in sign in the middle portion to become positive on the front side and negative on the rear side, turn to be positive on both sides further towards the trailing edge and then decrease and become mildly negative on the front side at the trailing edge. The net C_{Ls} is 0.09.

In spite of the lift mechanisms between the advanced and delayed rotations being different at turning, the difference in $\bar{C}_{Lv}(=0.075)$ is not large, compared to the differences in $\bar{C}_{La}(=0.260)$ and $\bar{C}_{Ls}(=0.127)$. However, the volume vortex lift $\bar{C}_{Lv}$ is the dominant factor that yields a high lift, in that if $\bar{C}_{Lv}$ is decreased significantly by altering the flow parameters, then neither $\bar{C}_{La}$ nor $\bar{C}_{Ls}$ can compensate the loss of $\bar{C}_{Lv}$. This can be seen by re-examining the values in table 1. If a higher lift is concerned, the delayed rotation with more negative δ is rejected by all the key components $\bar{C}_{La}$, $\bar{C}_{Ls}$ and $\bar{C}_{Lv}$ which decrease significantly with decreasing the phase δ from $-\pi/4$

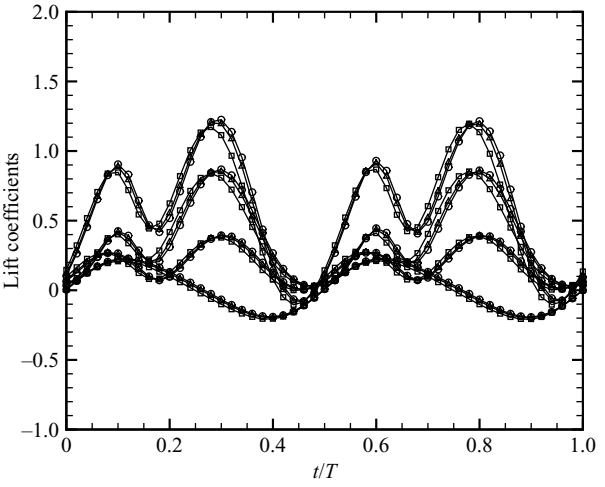

FIGURE 7. The time histories of the lift contribution for wing rotation about different chord lengths from the leading edge (□, 1/2 chord; △, 1/3 chord; ○, 1/4 chord).

to $-3\pi/8$ to $-\pi/2$. The advanced rotation with more positive δ will be rejected by both $\bar{C}_{Lv}$ and $\bar{C}_{Ls}$ which drop tremendously as δ goes up from $\pi/4$ to $3\pi/8$ and then to $\pi/2$ despite that $\bar{C}_{La}$ can be increased by increasing δ. Hence, the optimal range for δ is the range for which $\bar{C}_{Lv}$ is the dominant factor for high lift, while a slight adjustment of δ can be made to increase $\bar{C}_{La}$ and $\bar{C}_{Ls}$ without reducing $\bar{C}_{Lv}$ substantially.

4.1.2. *Influence of the rotational axis*

The effect of rotation is also examined by considering three axes of rotation for the symmetric motion. Their distances from the leading edge of the elliptic wing are respectively 1/2, 1/3 and 1/4 chord lengths. Figure 7 shows the time histories of the total lift C_L as well as three contributing components C_{La}, C_{Lv} and C_{Ls}. The trends of the total lift and all the lift components are quite similar, but we also observe that there is a phase delay if we move the axis from 1/2 chord length to 1/3 chord length or 1/4 length. Other minor differences caused by moving the axis closer to the leading edge include slight increases in all the force components: $\bar{C}_{La} = 0.0$, 0.014, 0.021; $\bar{C}_{Lv} = 0.364$, 0.365, 0.373; and $\bar{C}_{Ls} = 0.184$, 0.185, 0.190. The corresponding averaged total lifts are respectively 0.550, 0.564 and 0.581. In summary, the overall behaviours in the total lift and the force components do not differ qualitatively except for minor changes in magnitude.

4.1.3. *Influence of the Reynolds number*

In general, an insect exploits unsteady aerodynamic mechanisms over the range $Re = 10^2$–10^4 (Weis-Fogh 1973). For the hovering flight of a fruit fly, the order of the Reynolds number is around 100. In this study, Re is ranged between 57 and 129 to investigate the dependence of the averaged total lift as well as the four lift contributions over a time period. In particular, we should realize the important contribution of $\bar{C}_{Ls}$ from the surface vorticity in this relatively low Reynolds number region. The results are listed in table 2. In the entire range of investigation, $\bar{C}_{Lm}$ is negligible compared to other lift components and $\bar{C}_{La}$ is zero because of symmetric motion. In this table, we have all the lift force minima at $Re = 57$: $\bar{C}_L = 0.495$, $\bar{C}_{Lv} = 0.286$ and $\bar{C}_{Ls} = 0.208$. It is noted that the relative importance of

Re	$\bar{C}_L$	$\bar{C}_{Lm}$	$\bar{C}_{La}$	$\bar{C}_{Lv}$	$\bar{C}_{Ls}$	$\bar{C}_{Ls}+\bar{C}_{Lv}$
57	0.495	0.001	0	0.286	0.208	0.494
72	0.570	0.002	0	0.330	0.238	0.568
86	0.592	0.002	0	0.355	0.235	0.590
101	0.579	0.002	0	0.364	0.213	0.577
115	0.547	0.002	0	0.361	0.184	0.545
129	0.516	0.002	0	0.357	0.157	0.514

TABLE 2. Various time-averaged lift coefficients versus Re for fruit fly hovering with $\delta = 0$.

$\bar{C}_{Ls}$ measured by $\bar{C}_{Ls}/(\bar{C}_{Lv}+\bar{C}_{Ls})$ at this Reynolds number is high (42.1 %), and so the corresponding importance of $\bar{C}_{Lv}$ is 57.9 %. But neither the total lift nor any force component can be increased monotonically by increasing the Reynolds number. The surface vorticity lift $\bar{C}_{Ls}$ attains its maximum 0.238 at $Re = 72$; the volume vorticity lift $\bar{C}_{Lv}$ attains its maximum 0.364 at $Re = 101$; while the total lift $\bar{C}_L$ attains its maximum 0.592 at the intermediate $Re = 86$. But there is still a trend with increase in the Reynolds number. The relative importance of $\bar{C}_{Ls}$ measured by $\bar{C}_{Ls}/(\bar{C}_{Lv} + \bar{C}_{Ls})$ decreases monotonically to 30.6 % at $Re = 129$, and the corresponding importance of $\bar{C}_{Lv}$ increases to 69.4 %. In summary, the total force $\bar{C}_L$ as well as the vorticity force $\bar{C}_{Lv}$ cannot be increased monotonically with increasing the Reynolds number, though the contribution of $\bar{C}_{Lv}$ relative the surface vorticity lift $\bar{C}_{Ls}$ is indeed increased.

4.2. *Model for dragonfly motion*

The motion for dragonfly is performed with $A_0^*/c^* = 2.5$ and $f^* = 40$ Hz. The stroke plane inclines to the horizontal with an angle $\beta = \pi/3$. The Reynolds number Re is 157. The motion of the wing elliptic with aspect ratio 8 is given by $A(t) = A_0/2\,[(\cos(2\pi f t) - 1)]$. The rotation is about the middle chord of the wing, and the angle of attack is $\alpha(t) = \pi/4 - \pi/4[\sin(2\pi f t + \delta)]$. The simulated motion is started from rest, and the lift reaches a stationary state after five strokes. Here we choose the tenth period for investigation.

4.2.1. *Influence of the phase difference between translation and rotation*

Figure 8 shows the average total lift $\bar{C}_L$ as well as the four lift components $\bar{C}_{Lm}$, $\bar{C}_{La}$, $\bar{C}_{Lv}$ and $\bar{C}_{Ls}$ versus the phase difference δ. The average lift $\bar{C}_L$ has the maximum ($= 0.705$) in a range near $\delta = \pi/4$, decaying from both sides of $\delta = \pi/4$ to 0.017 at $\delta = -\pi/4$ and to 0.534 at $\delta = \pi/2$. This behaviour of $\bar{C}_L$ can be analysed by examining the various contributions of the constituent force components. The lift $\bar{C}_{Lm}$ is uniformly small for all δ but decreases slightly with increasing the phase difference. By increasing the phase difference, the lift component $\bar{C}_{La}$ is increased almost steadily from -0.211 at $\delta = -\pi/4$ to 0 at $\delta = 0$ and then to 0.304 at $\delta = \pi/2$. The volume vorticity lift $\bar{C}_{Lv}$ has the maximum 0.439 at $\delta = 0$, decaying from both sides of $\delta = 0$ to 0.226 at $\delta = -\pi/4$ and to 0.153 at $\delta = \pi/2$. By increasing the phase difference, the surface vorticity lift $\bar{C}_{Ls}$ increases gradually from -0.019 at $\delta = -\pi/4$ to 0.132 at $\delta = 0$, attaining the maximum 0.155 at $\delta = 5\pi/18$ and then decaying gradually to 0.107 at $\delta = \pi/2$. As the phase difference δ is increased above $\pi/3$ the lift $\bar{C}_{La}$ begins to outweigh $\bar{C}_{Lv}$ and equals in magnitude to the total vortex lift, i.e. the sum of $\bar{C}_{Lv}$ and $\bar{C}_{Ls}$ at $\delta = 4\pi/9$. It is of interest to notice that for the symmetric rotation ($\delta = 0$) the average total lift $\bar{C}_L$ is completely credited to the vortex force, that is $\bar{C}_{Lv}$ (76.6 %) + $\bar{C}_{Ls}$ (22.9 %), as other force components have negligible contributions at this mode of motion. However, the average total lift $\bar{C}_L$ does not have the maximum at $\delta = 0$ but

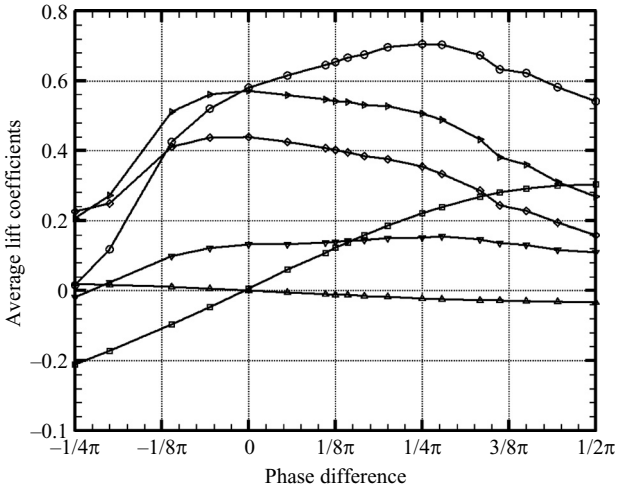

FIGURE 8. The average lift coefficients versus phase difference δ ($\circ$, C_L; $\triangle$, C_{Lm}; $\square$, C_{La}; $\diamond$, C_{Lv}; $\triangledown$, C_{Ls}; $\triangleright$, $\bar{C}_{Ls}+\bar{C}_{Lv}$).

at the advanced rotation with $\delta = \pi/4$. In other words, the optimal flight of dragonfly for a higher lift favours the advanced rotation with $\delta = \pi/4$ rather than the symmetric rotation. More precisely in magnitude, the dragonfly switches from the symmetric rotation to the advanced, gaining $\bar{C}_{La}$ by 0.221 at the expense of sacrificing the vortex lift $\bar{C}_{Lv}+\bar{C}_{Ls}$ by -0.066. Nevertheless, an advanced rotation with even larger δ is rejected because the rate of decrease in the vortex lift $\bar{C}_{Lv}+\bar{C}_{Ls}$ exceeds the rate of increase in $\bar{C}_{La}$.

Next, we turn to examine the unsteady behaviours. In the following discussion, we shall consider more details only for three phase differences: $\delta = 0$ (symmetric), $\pi/5$ (advanced) and $-\pi/5$ (delayed). Figures 9–11 show the time-varying total lift coefficient C_L as well as the four constituent lift coefficients for the symmetric, advanced and delayed rotations, respectively, over a full time period. The wing is in downstroke during the first half of time period and in upstroke during the latter half of time period. First, we note that C_{Lm} is uniformly small all the time for all the types of motion. Next, we observe that C_{La} is negative during the middle time period from $t/T = 0.25$ to $t/T = 0.75$ and positive during the rest of the time period. The C_{La} for the symmetric rotation has odd symmetry in time, yielding net zero $\bar{C}_{La}$. For the advanced rotation, the average of C_{La} in the positive phase is larger than that in the negative phase in magnitude; the opposite holds for the delayed rotation. These differences result in the positive $\bar{C}_{La} = 0.185$ for the advanced rotation and negative $\bar{C}_{La} = -0.173$ for the delayed rotation. Then, we turn to the more interesting behaviours of C_{Lv}. Roughly speaking, the lift C_{Lv} is positive most of time in the downstroke phase and during a later time period of the upstroke phase. More precisely, the time intervals for positive C_{Lv} are (0.024, 0.616) and (0.72, 0.816) for the symmetric rotation, (0.064, 0.584) for the advanced rotation and (0.96, 1) (0, 0.504) for the delayed rotation. The volume vortex lift C_{Lv} oscillates in a smaller range from 1.51 at $t/T = 0.28$ to -0.212 at $t/T = 0.92$ for the symmetric rotation, in the range from 2.43 at $t/T = 0.3$ to -1.07 at $t/T = 0.868$ for the advanced rotation and in a larger range from 3.58 at $t/T = 0.196$ to -1.67 at $t/T = 0.648$ for delayed rotation. It is important to note that for the symmetric rotation, the lift C_{La} is in the upstroke motion when the negative is small in magnitude. As a comparison, the

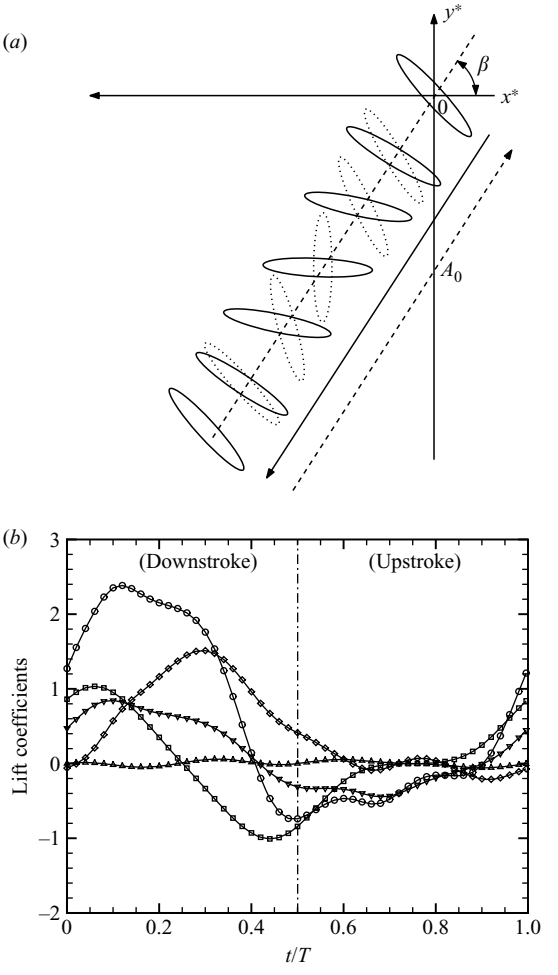

FIGURE 9. (*a*) Model 2 for the symmetric rotation with $\delta = 0$ at $Re = 157$. (*b*) The time histories of the lift contribution (○, C_L; △, C_{Lm}; □, C_{La}; ◇, C_{Lv}; ▽, C_{Ls}).

insect wing in advanced rotation loses C_{Lv} significantly in the latter half of upstroke motion, and therefore the advanced rotation has a smaller $\bar{C}_{Lv}$ than the symmetric rotation. Another comparison shows that the delayed rotation has an even smaller $\bar{C}_{Lv}$ compared to the symmetric rotation, as the wing loses more volume vortex lift in the stage of upstroke motion. It is also of interest to observe that the sign of C_{Ls} is almost all the time the same as that of the total lift C_L. The total lift C_L oscillates in a smaller range from 2.384 at $t/T = 0.12$ to -0.746 at $t/T = 0.492$ for the symmetric rotation, in the range from 3.067 at $t/T = 0.268$ to -1.174 at $t/T = 0.832$ for the advanced rotation and in a larger range from 5.193 at $t/T = 0.188$ to -2.588 at $t/T = 0.642$ for the delayed rotation.

The time intervals during which the insect wing gains a positive C_L are (0.904, 1) (0, 0.408) for the symmetric rotation, (0.92, 1) (0, 0.456) for the advanced rotation and (0.928, 1) (0, 0.328) for the delayed rotation. In summary, C_{La} and C_{Ls} are positive initially at $t/T = 0$, while C_{Lv} is slightly negative. As time increases, the volume vortex lift C_{Lv} begins to increase its contribution and does so up to the time at which the wing is in the horizontal position and then decreases as the wing lifts again its angle

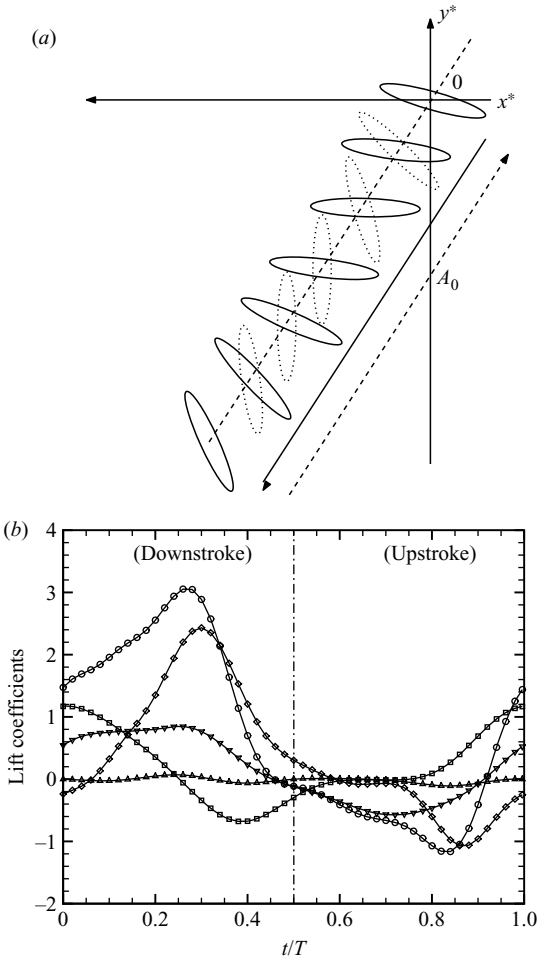

FIGURE 10. (*a*) Model 2 for the advanced rotation with $\delta = \pi/5$. (*b*) The time histories of the lift contribution (○, C_L; △, C_{Lm}; □, C_{La}; ◇, C_{Lv}; ▽, C_{Ls}).

of attitude but remaining positive for the entire downstroke stage. However, the C_{La} begins to sink below 0 at $t/T = 0.25$ and attains its minimum at $t/T = 0.44$ for the symmetric rotation, at $t/T = 0.388$ for the advanced rotation and at $t/T = 0.488$ for the delayed rotation. Hence, the total lift C_L sustains a shorter time interval of positive values than the vortex lift C_{Lv} in the downstroke motion. The situation for the upstroke motion is more complicated. In the first half of upstroke motion, the lift components C_{La} and C_{Ls} are negative. The lift component C_{Lv} is mildly small in the entire phase of upstroke for the symmetric rotation, substantially negative in the latter half of downstroke for the advanced rotation and substantially negative in the former half of downstroke for the delayed rotation. The total lift coefficient C_L for all types of motion rises above zero earlier than C_{Lv} does in a later stage of downstroke.

Figure 12(*a–e*) shows the various snapshots of vorticity and vortex lift elements at five different instants during a time period for the symmetric rotation. The sequence starts with the time instant at which the insect wing is in the beginning of downstroke. At $t/T = 0$, there are already two detached vortices of different signs in the flow, one in front of the wing and the other near the trailing edge. The detached vortex near

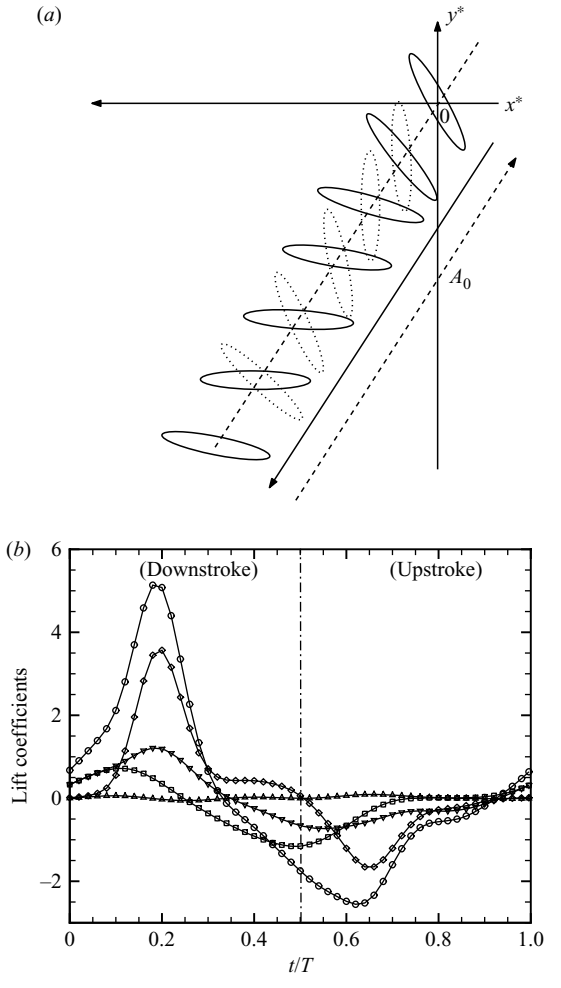

FIGURE 11. (*a*) Model 2 for the delayed rotation with $\delta = -\pi/5$. (*b*) The time histories of the lift contribution ($\circ$, C_L; $\triangle$, C_{Lm}; $\square$, C_{La}; $\diamond$, C_{Lv}; $\triangledown$, C_{Ls}).

the trailing edge contributes positive lift elements, while the front vortex contributes negative lift elements more than the positive ones. There are also two slender regions of vorticity of different signs closely attached to the body; their contributions to positive and negative lift elements tend to cancel each other ($C_{Lv} = -0.06$). As time increases, the insect wing moves downward along $\beta = \pi/3$ while rotating counterclockwise simultaneously. Intense vorticity is generated from the leading and trailing edges. Also, there are slender vortices on the back of the body. The detached front vortex is now merged with the trailing edge vortex, while the detached trailing vortex is pushed further away from the body and weakens in strength because of diffusion. The newly generated vortices are more effective in contributing to intensive positive lift elements. By time $t/T = 0.16$, we have $C_{Lv} = 0.95$. This trend or behaviour continues as time further increases. The leading and trailing vortices are further intensified, and by $t/T = 0.28$ we have the maximum $C_{Lv} = 1.51$. Then still in downstroke, the wing begins to rotate clockwise, and both the leading and trailing edges are no longer supplied with further vorticity, weakening in strength and being ready to detach from

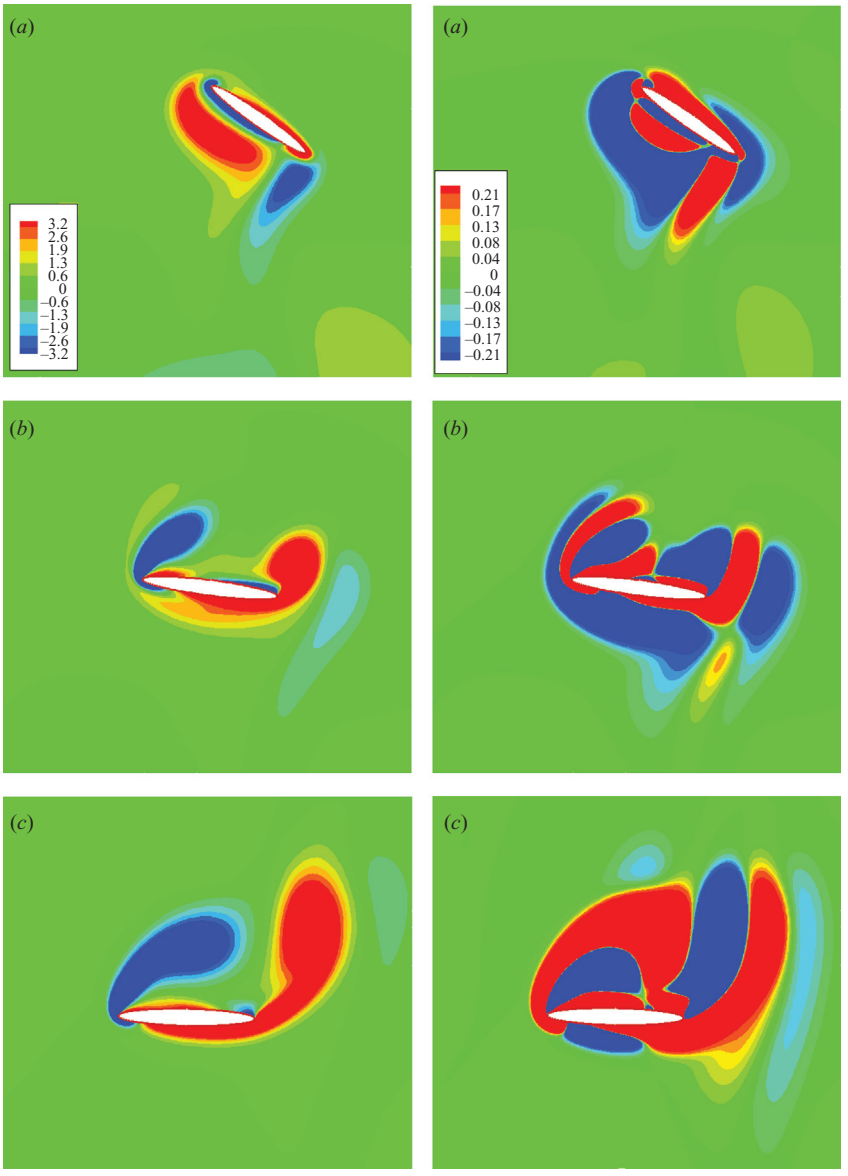

FIGURE 12. For legend see facing page.

the insect wing. The vortex lift C_{Lv} therefore decreases, and by $t/T = 0.48$ we have $C_{Lv} = 0.47$. In table 3, total average lift and its four components for the downstroke and upstroke phases are listed.

Unlike the previous model for fruit fly, the current model also exhibits a drag (thrust) component. As an illustration, figure 13 shows the time histories of the total drag C_D and its four constituent components C_{Dm}, C_{Da}, C_{Dv} and C_{Ds} for the symmetric rotation. It is seen that the insect gains thrust in the half period form $t/T = 0.39$ to $t/T = 0.92$ (mostly in the phase of upstroke) and experiences drag in the rest of the motion. The net budget is the thrust $-\bar{C}_D = 0.304$. Among the four drag components, C_{Dm} is relatively small but oscillates with a larger amplitude

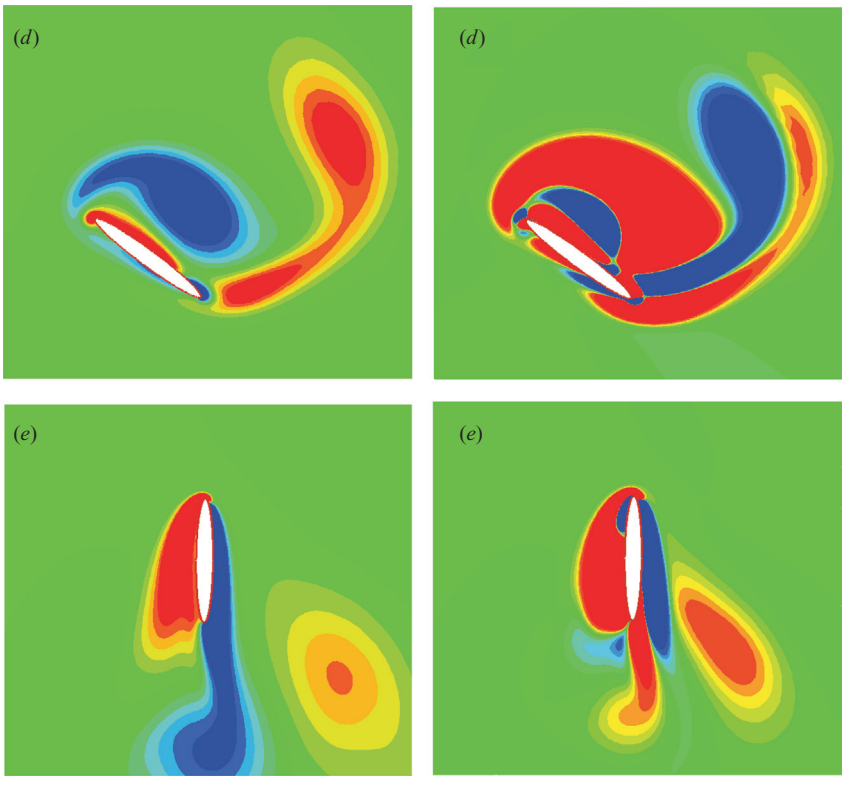

FIGURE 12. Selected plots of vorticity and lift elements for the symmetric motion with $\delta = 0$. Left: vorticity contour (red, anticlockwise; blue, clockwise). Right: lift force element contour (red, positive lift elements; blue, negative lift elements). (*a*) $t/T = 0$, $\alpha(t) = 45°$, $v = 0$; (*b*) $t/T = 0.16$, $\alpha(t) = 7.0°$, $v = -0.84$; (*c*) $t/T = 0.28$, $\alpha(t) = 0.8°$, $v = -0.98$; (*d*) $t/T = 0.48$, $\alpha(t) = 39.4°$, $v = -0.12$; (*e*) $t/T = 0.76$, $\alpha(t) = 89.9°$, $v = 0.998$.

δ	$\alpha(0)$	Phase	$\bar{C}_L$	$\bar{C}_{Lm}$	$\bar{C}_{La}$	$\bar{C}_{Lv}$	$\bar{C}_{Ls}$
$\pi/5$	18.5°	Downstroke	0.889	−0.001	0.067	0.539	0.284
		Upstroke	−0.198	−0.016	0.118	−0.167	−0.133
0	45°	Downstroke	0.677	0.002	0.005	0.440	0.230
		Upstroke	−0.103	0.001	−0.005	0.0004	−0.099
$-\pi/5$	71.5°	Downstroke	0.678	0.003	−0.056	0.531	0.200
		Upstroke	−0.562	0.014	−0.117	−0.282	−0.177

TABLE 3. Various time-averaged lift coefficients versus δ for each half stroke at $Re = 157$.

in the phase of upstroke, and the net $-\bar{C}_{Dm} = 0.004$. The component C_{Da} provides thrust in the middle rang from $t/T = 0.25$ to $t/T = 0.75$ and drag in the rest of the time, and the net contribution is zero. The component C_{Ds} provides more thrust at $t/T = 0.39$ and $t/T = 0.95$ and then drag in the rest of time, and the net budget is $-\bar{C}_{Ds} = 0.142$. From $t/T = 0.65$ to $t/T = 0.036$, the insect wing experiences drag from the component C_{Dv}. The most significant $\bar{C}_{Dv}$ for thrust occurs when the insect wing turns from lifting its angle of attitude to lowering the angle in the phase of

δ	$\alpha(0)$	Phase	$\bar{C}_D$	$\bar{C}_{Dm}$	$\bar{C}_{Da}$	$\bar{C}_{Dv}$	$\bar{C}_{Ds}$
$\pi/5$	18.5°	Downstroke	0.184	0.005	−0.103	0.212	0.070
		Upstroke	−0.483	−0.020	−0.001	−0.285	−0.177
0	45°	Downstroke	0.136	0.000	0.002	0.078	0.056
		Upstroke	−0.440	−0.004	−0.002	−0.236	−0.198
$-\pi/5$	71.5°	Downstroke	0.478	−0.005	0.108	0.204	0.171
		Upstroke	−0.712	0.012	−0.010	−0.530	−0.184

TABLE 4. Various time-averaged drag coefficients versus δ for each half stroke at $Re = 157$.

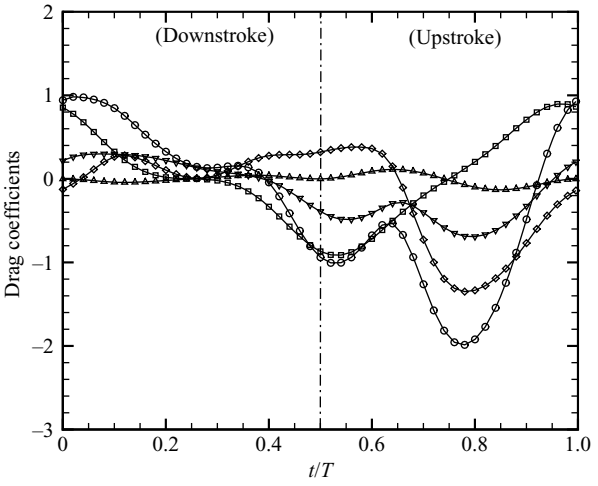

FIGURE 13. The time histories of the drag contribution for the symmetric rotation with $\delta = 0$ ($\circ$, C_D; $\triangle$, C_{Dm}; $\square$, C_{Da}; $\diamond$, C_{Dv}; $\triangledown$, C_{Ds}).

upstroke. The net budget is $-\bar{C}_{Dv} = 0.158$. In table 4, total average drag and its four components for the downstroke and upstroke phase.

If we look into the surface lift elements for symmetric rotation, there are two distinguished distributions associated with the horizontal and vertical positions of the wing. It either case, the lift elements are much larger in magnitude at the leading edge than at the rest of the wing surface. As the wing is in the horizontal position ($t/T = 0.25$) in figure 9, the lift elements are negligibly small in the middle parts of both the lower and upper sides and are largely positive around the leading edge. Near the trailing edge the lift elements are mildly positive on the lower side and mildly negative but smaller in magnitude on the upper side. The net C_{Ls} is 0.61. When the wing is in the vertical position ($t/T = 0.75$), the lift elements on the front side are largely negative at the leading edge and become small but still negative further toward s and till the trailing edge. On the rear side, the lift elements are largely positive at the leading edge and become mildly negative towards and till the trailing edge. The net C_{Ls} is −0.33.

4.2.2. *Influence of the Reynolds number*

For the hovering flight of a fruit fly, the order of Re is between 10^2 and 10^3. It was shown that the averaged force is independent of Re when $150 < Re < 1256$ (Wang 2000*a*). In the present study, the Reynolds number is varied from 75 to 628 for the symmetric motion to investigate the total lift as well as the four contributing

Re	$\bar{C}_L$	$\bar{C}_{Lm}$	$\bar{C}_{La}$	$\bar{C}_{Lv}$	$\bar{C}_{Ls}$	$\bar{C}_{Ls}+\bar{C}_{Lv}$
75	0.445	0.000	0	0.301	0.144	0.445
157	0.572	0.001	0	0.440	0.131	0.571
225	0.584	0.001	0	0.471	0.112	0.583
314	0.605	0.001	0	0.500	0.104	0.604
450	0.606	0.002	0	0.513	0.091	0.604
628	0.601	0.002	0	0.522	0.077	0.599

TABLE 5. Various time-averaged lift coefficients versus Re for dragonfly hovering with $\delta = 0$.

components. The results are listed in table 5. The averaged total lift $\bar{C}_L$ increases by 28.54 % with increasing Re from 75 to 157, then increases mildly by 5.8 % with increasing Re from 157 to 314 and has approximately the same value with further increasing Re from 314 to 628. Again, we see negligible contribution from $\bar{C}_{Lm}$ in the range of investigation and identically zero $\bar{C}_{La}$ because of the symmetric motion. Of more interest is the significant increase of the averaged volume vorticity lift $\bar{C}_{Lv}$ and decrease of the averaged surface vorticity lift $\bar{C}_{Lv}$. It is seen that $\bar{C}_{Lv}$ increases very significantly by 46.18 % with increasing Re from 75 to 157 and also substantially by 18.64 % with increasing Re from 157 to 628. On the other hand, $\bar{C}_{Ls}$ decreases by 9.03 % with increasing Re from 75 to 157 and by 41.2 % with increasing Re from 157 to 628. As a result, the relative importance of $\bar{C}_{Lv}$ measured by $\bar{C}_{Lv}/(\bar{C}_{Lv}+\bar{C}_{Ls})$ increases from 67.6 % to 87.1 %, and correspondingly that of $\bar{C}_{Ls}$ measured by $\bar{C}_{Ls}/(\bar{C}_{Lv}+\bar{C}_{Ls})$ decreases from 32.4 % to 12.9 %. The opposite trends of $\bar{C}_{Lv}$ and $\bar{C}_{Ls}$ present their much more significant dependence on the Reynolds number compared to the total lift $\bar{C}_{Lv}$. It is also worthwhile to remark that for the symmetric motion even with different Reynolds numbers, the averaged total lift is almost entirely credited to the vorticity lift (volume plus and surface vorticity lift).

4.2.3. *Influence of the wing shape*

The wing shapes we chose and shown in figure 14 can be categorized into two types. One type is the symmetric shape like 1/8, 1/10 and 1/12 thick ellipses as well as NACA0012 airfoil. The other type is N-10, S1223 and CLARK-V which can be sub-divided to those with a blunt nose and more or less cambered. The performance of the seven wing shapes is illustrated for the symmetric hovering motion of dragonfly at $Re = 157$. Table 6 shows the total as well as the contributing time-averaged lift coefficients. First, the results for the ellipses of different thickness are compared. The averaged $\bar{C}_{Lm}$ is small and can be neglected, and $\bar{C}_{La}$ is zero for symmetric motion. On the other hand, both vorticity lift contributions $\bar{C}_{Lv}$ and $\bar{C}_{Ls}$ can be increased slightly by decreasing the thickness of elliptic wing. If we consider the wings of 1/8 and 1/12 thickness, there is only 1.59 % gain in $\bar{C}_{Lv}$, and, however, the increase in $\bar{C}_{Ls}$ runs up to 6.87 %. Because of the relatively small importance of $\bar{C}_{Ls}$ compared to $\bar{C}_{Lv}$, the total averaged lift $\bar{C}_L$ only increases by 2.8 % with decreasing the thickness of wing from 1/8 to 1/12. The NACA0012 airfoil has the advantage of improving the volume vorticity lift $\bar{C}_{Lv}$ at a smaller expense of loosing $\bar{C}_{Ls}$. The increase in $\bar{C}_{Lv}$ is 0.045, and the decrease in $\bar{C}_{Ls}$ is -0.024 compared to the 1/12 thickness wing. Meanwhile, we also see an increased contribution from $\bar{C}_{Lm}$ by 0.003. The resultant gain in the averaged total lift $\bar{C}_L$ is 4.08 %.

The more interesting comparisons are between the symmetric and non-symmetric or cambered airfoils. The non-symmetric wings have larger $\bar{C}_L$ and $\bar{C}_{Lv}$ but smaller

Shape	$\bar{C}_L$	$\bar{C}_{Lm}$	$\bar{C}_{La}$	$\bar{C}_{Lv}$	$\bar{C}_{Ls}$	$\bar{C}_{Ls}+\bar{C}_{Lv}$
Elliptic 1/8	0.572	0.001	0	0.440	0.131	0.571
Elliptic 1/10	0.579	0.001	0	0.443	0.135	0.578
Elliptic 1/12	0.588	0.001	0	0.447	0.140	0.587
NACA 0012	0.612	0.004	0	0.492	0.116	0.608
CLARK-V	0.628	0.003	0.007	0.505	0.113	0.618
N-10	0.658	0.010	0.007	0.525	0.116	0.641
S1223	0.673	0.006	0.008	0.564	0.095	0.659

TABLE 6. Various time-averaged lift coefficients versus wing shape for dragonfly hovering with $\delta = 0$ at $Re = 157$.

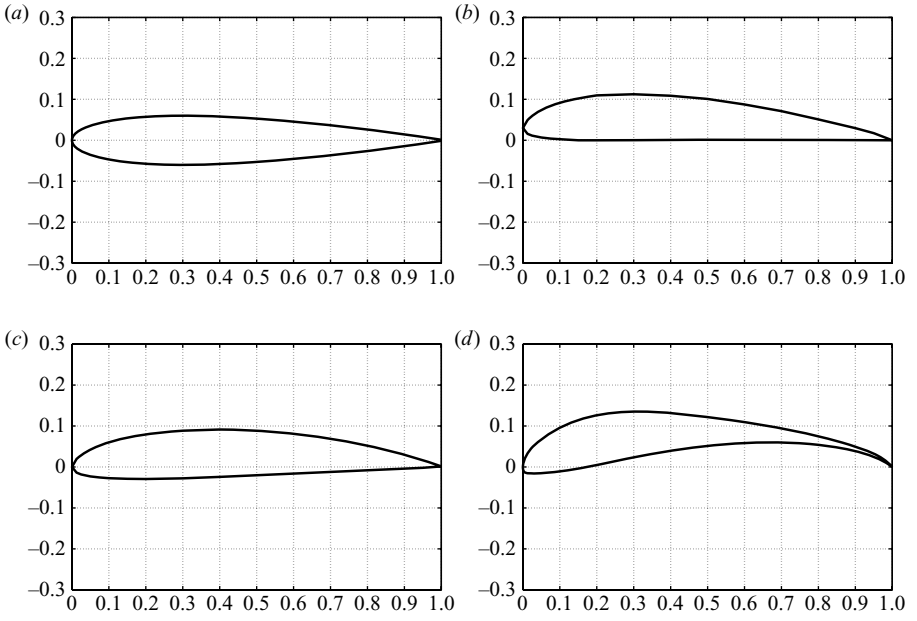

FIGURE 14. The various wing profiles: (*a*) NACA0012 (upper–lower symmetric), (*b*) N-10 (slightly cambered), (*c*) CLARK-V (slightly cambered), (*d*) S1223 (largely cambered) (UIUC Airfoils Coordinates Database).

$\bar{C}_{Ls}$ compared to the symmetric wings. For example, if we replace the 1/12 thickness ellipse with the N-10 wing, the gain in C_{Lv} is 0.078, while the loss in $\bar{C}_{Ls}$ is −0.024. Meanwhile, we also see the contribution from $\bar{C}_{Lm}$ increased by 0.009. As a result, the gain in the total averaged lift $\bar{C}_L$ is 11.9 %. The performance of CLARK-V wing lies between those of NACA0012 airfoil and N-10 airfoil. As far as a favourable lift is concerned, the S1223 wing shape is most advantageous. Again, we compare it to the 1/12 thickness ellipse. The lift $\bar{C}_{Lv}$ is increased very significantly by 0.117, while $\bar{C}_{Ls}$ is decreased by 0.045. The relative importance of $\bar{C}_{Lv}$ measured by $\bar{C}_{Lv}/(\bar{C}_{Lv}+\bar{C}_{Ls})$ increases from 76.1 % to 85.6 %, and correspondingly that of $\bar{C}_{Ls}$ measured by $\bar{C}_{Ls}/(\bar{C}_{Lv}+\bar{C}_{Ls})$ decreases from 23.9 % to 14.4 %. The resultant gain in the averaged total lift $\bar{C}_L$ is 14.5 %.

In order to examine the effects of unsteadiness, we also show time histories of C_{Lv} and C_{Ls} in a period of time of symmetric motion for all types of airfoils in

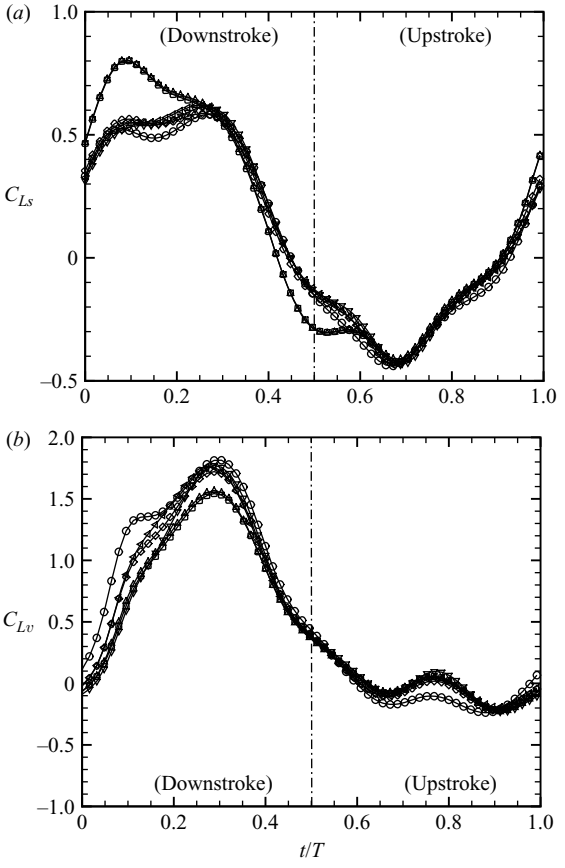

FIGURE 15. (*a*) The time histories of C_{Lv}. (*b*) The time histories of C_{Ls} (□, 1/10 thick ellipse; △, 1/12 thick ellipse; ▽, NACA0012; ◁, N-10; ◇, CLARK-V; ○, S1223).

figure 15. It is first noted that the 1/10 and 1/12 thick ellipses have almost identical trends in both C_{Ls} and C_{Lv} for the entire period of motion, while the S1223 airfoil exhibits the largest deviations. The S1223 airfoil has uniformly higher C_{Lv} in the entire downstroke phase and relatively lower C_{Lv} in the middle of upstroke phase. The NACA0012 airfoil exhibits the major difference in C_{Lv} from those of the ellipses in a middle range of downstroke phase. The behaviours of C_{Lv} for the other two types of airfoils – N-10 and CLARK-V – lie in between those of S1223 and NACA0012. In other words, the other types of airfoils compared to the ellipses gain extra volume vorticity lift C_{Lv} mainly from the downstroke motion. On the contrary, the other types of airfoils compared to the ellipses lose the surface vorticity lift C_{Ls} substantially in the first half of downstroke motion but have a little bit higher C_{Ls} at the turning from downstroke to upstroke.

5. Concluding remarks

It has been of great interest to understand how insect flight benefits from unsteady aerodynamics. In this study, we have taken the viewpoint of force decomposition to examine the lift by its four contributions from unsteadiness. In particular, we have considered the simplified hovering models of Dickinson *et al.* (1999) and Wang (2000)

for the fruit fly and dragonfly. The force components of the total lift C_L for the present applications include the volume vorticity lift C_{Lv} and the surface vorticity lift C_{Ls} and two credited to the surface motion – C_{Lm} associated with the wing velocity and C_{La} associated with the wing acceleration. The two latter components C_{Lm} and C_{La} are determined once the geometry and the hovering motion are prescribed, while the former two C_{Lv} and C_{Ls} can be determined only when the flow field is solved or measured.

It was observed that C_{Lm} is uniformly small in time for all the types of motions and can be neglected in the discussion. For flights at the low Reynolds numbers $Re = 115$ (fruit fly) and $Re = 157$ (dragonfly), the surface vorticity contribution C_{Ls} is important. The interplay between the three major force components C_{La}, C_{Lv} and C_{Ls} constitutes a plethora of interesting lift behaviours at various phases of motion. A mild change in $\bar{C}_L$ is often accompanied with more drastic changes in $\bar{C}_{Lv}$ and $\bar{C}_{Ls}$. The component $\bar{C}_{La}$ is increased by increasing the phase difference δ in the models of hovering, and on the contrary, $\bar{C}_{Lv}$ is maximal at $\delta = 0$ (symmetric rotation), and $\bar{C}_{Ls}$ has the maximum in an advanced rotation with an intermediate δ. For both models of hovering, as the net lift is concerned, the symmetric rotation is nearly fully supported by the vortex force ($\bar{C}_{Lv}$ plus $\bar{C}_{Ls}$). Moreover, among all the modes of hovering the net vortex lift (averaged over a time period) is maximal when the wing performs the symmetric rotation, but the optimal average lift is attained for an advanced rotation, which, compared to the symmetric rotation, increases the force contribution due to the unsteady surface motion at the expense of sacrificing contribution from the vorticity.

There are other interesting features concerning the contributions from the volume vorticity via lift elements. First, we summarize the results for fruit fly. The most efficient phase in generating positive lift elements is the time interval during which the wing drives with full speed. The C_{Lv} attained its maximum shortly after this moment. When turning from facing one direction to the opposite, the insect wing was shown to exhibit a mechanism – which we called 'riding on lift elements' – for the advanced rotation. This 'riding-on' effect corresponds to the phenomenon of 'wake capture' called by Dickinson *et al.* (1999). This is very important for the advanced rotation to remain in the phase of positive C_{Lv} in a time interval after turning. This mechanism is less visible for the symmetric rotation and does not appear in the delayed rotation. If we shift the axis of rotation, the time histories of the total lift and various lift components remain very similar except for minor differences in phase and magnitude. But if we vary the Reynolds number Re between 57 and 129, the insect wing attains the maximum averaged total lift at the intermediate $Re = 86$, though the relative importance of $\bar{C}_{Lv}$ to $\bar{C}_{Ls}$ increases with increasing the Reynolds number.

Next, we summarize the results for dragonfly. The lift component C_{Lv} is positive in almost the entire phase of downstroke, attaining its maximum at a moment close to the turn from lowering to lifting the wing's angle of attack. In the phase of downstroke, the symmetric rotation maintains small magnitude, while the advanced rotation loses the vortex lift significantly in the latter stage of downstroke, and the delayed rotation loses the vortex lift most of the time in the phase of downstroke. The lift component C_{La} becomes negative in the middle period, and thus the total lift C_L sustains its positive sign in a shorter time interval than C_{Lv}. If we vary the Reynolds number between 75 and 628, $\bar{C}_{Lv}$ will be increased substantially by increasing Re from 75 to 314 and slightly as Re is increased above 314. In other words, in the range of Re between 314 and 628, the total lift C_L is little dependent on Re because the increase in $\bar{C}_{Lv}$ is almost entirely balanced by the decrease in $\bar{C}_{Ls}$ as Re is increased. The effects of the wing profile have also been investigated. Seven types of wings were considered:

1/8, 1/10 and 1/12 thick ellipses, NACA0012 (symmetric wings), N-10, CLARK-V and S1223 (cambered wings). The performance of these wings improves with respect to the averaged total lift $\bar{C}_L$ by gaining more volume vorticity lift according to the order listed above. The time histories of the force components show that the cambered wings compared to the ellipses gain substantially C_{Lv} in the upstroke phase while losing less significantly C_{Ls} in the first half of upstroke.

Although the method of force decomposition analysed only two-dimensional flow in the present study, the formulation is general enough for applications to three-dimensional flow and flow about bodies in other types of motion. Unsteady aerodynamics for two wings (e.g. clap and fling) or more bodies (e.g. wing–body configuration) from the perspective of the diagnostic force theory are also worthy of investigation.

The authors would like to thank Professor Theodore Y. T. Wu of Caltech for his interest in our work and constant encouragement during the past years. We also thank Professor Jre-Zhi Wu of the University of Tennessee Space Institute for useful discussioins on various viewpoints of aerodynamic and hydrodynamic forces over the years. The work was supported in part by the National Science Council of the Republic of China (Taiwan) under contract nos. NSC97-2221-E-002-223-MY3 and NSC97-2221-E-002-048.

REFERENCES

Biesheuvel, A. & Hagmeijer, R. 2006 On the force on a body moving in a fluid. *Fluid Dyn. Res.* **38**, 716–742.

Bos, F. M., Lentink, D., Oudheusden, B. W. Van & Bijl, H. 2008 Influence of wing kinematics on aerodynamic performance in hovering insect flight. *J. Fluid Mech.* **594**, 341–368.

Burgers, J. M. 1920 On the resistance of fluids and vortex motion. *Proc. Kon. Akad. Westenschappen te Amsterdam* 774–782.

Chang, C. C. 1992 Potential flow and forces for incompressible viscous flow. *Proc. R. Soc.* A **437**, 517–525.

Chang, C. C. & Chern, R. L. 1991 A numerical study of flow around an impulsively started circular cylinder by a deterministic vortex method. *J. Fluid Mech.* **233**, 243–263.

Chang, C. C. & Lei, S. Y. 1996*a* On the sources of aerodynamic forces: steady flow around a sphere or a cylinder. *Proc. R. Soc.* A **452**, 2369–2395.

Chang, C. C. & Lei, S. Y. 1996*b* An analysis of aerodynamic forces on a delta wing. *J. Fluid. Mech.* **316**, 173–196.

Chang, C. C., Yang, S. H. & Chu, C. C. 2008 A many-body force decomposition with applications to flow about bluff bodies. *J. Fluid Mech.* **600**, 95–104.

Chu, C. C., Chang, C. C., Liu, C. C. & Chong, R. L. 1996 Suction effect on an impulsively started circular cylinder: vortex structure and drag reduction. *Phys. Fluids* **8**, 2995–3007.

Dickinson, M. H. 1994 The effects of wing rotation on unsteady aerodynamic performance at low Reynolds number. *J. Exp. Biol.* **192**, 179–206.

Dickinson, M. H. & Götz, K. G. 1993 Unsteady aerodynamic performance of model wings at low Reynolds numbers. *J. Exp. Biol.* **174**, 45–64.

Dickinson, M. H., Lehmann, F. O. & Sane, S. P. 1999 Wing rotation and the aerodynamic basis of insect flight. *Science* **284**, 1954–1960.

Ellington, C. P. 1984 The aerodynamics of hovering insect flight. *Phil. Trans. R. Soc. Lond.* B **305**, 1–181.

Ellington, C. P., van den Berg, C., Willmott, A. P. & Thomas, A. L. R. 1996 Leading-edge vortices in insect flight. *Nature* **384**, 626–630.

Howarth, L. 1935 The theoretical determination of the lift coefficient for a thin elliptic cylinder. *Proc. R. Soc. London.* A **149**, 558–586.

Howe, M. S. 1989 On unsteady surface forces, and sound produced by the normal chopping of a rectilinear vortex. *J. Fluid Mech.* **206**, 131–153.

Howe, M. S. 1995 On the force and moment on a body in an incompressible fluid, with application to rigid bodies and bubbles at high and low Reynolds numbers. *Quart. J. Mech. Appl. Math.* **48**, 401–426.

Howe, M. S., Lauchle, G. C. & Wang, J. 2001 Aerodynamic lift and drag fluctuations of a sphere. *J. Fluid Mech.* **436**, 41–57.

Isogai, K., Fujishiro, Saitoh, T., Yamamoto, M., Yamasaki, M. & Matsubara, M. 2004 Unsteady three-dimensional viscous flow simulation of a dragonfly hovering. *AIAA J.* **42**, 2053–2059.

Kambe, T. 1986 Acoustics emissions by vortex motions. *J. Fluid Mech.* **173**, 643–666.

Landau, L. D. & Lifshitz, E. M. 1987 *Fluid Mechanics* (2nd ed.) Pergamon.

Lehmann, F. O. 2008 When wings touch wakes: understanding locomotor force control by wake–wing interference in insect wings. *J. Exp. Biol.* **211**, 224–233.

Lighthill, M. J. 1973 On Weis-Fogh mechanism of lift generation. *J. Fluid Mech.* **60**, 1–17.

Lighthill, M. J. 1979 Wave and hydrodynamic loading. *Proc. Second Intl Conf. Behaviour Off-Shore Struct., BHRA Cranfield*, **1**, 1–40.

Lighthill, M. J. 1986 Fundamentals concerning wave loading on offshore structures. *J. Fluid Mech.* **173**, 667–681.

Maxworthy, T. 1979 Experiments on the Weis-Fogh mechanism of lift generation by insects in hovering flight. Part 1. Dynamics of the fling. *J. Fluid Mech.* **93**, 47–63.

Ragazzo, C. G. & Tabak, E. G. 2007 On the force and torque on systems of rigid bodies: a remark on an integral formula due to Howe. *Phys. Fluids*, **19**, 057108.

Ramamurti, R. & Sandberg, W. C. 2002 A three-dimensional computational study of the aerodynamic mechanisms of insect flight. *J. Exp. Biol.* **205**, 1507–1518.

Rayner, J. M. V. 1979 A vortex theory of animal flight. Part 1. The vortex wake of a hovering animal. *J. Fluid Mech.* **91**, 697–730.

Sane, S. P. 2003 The aerodynamics of insect flight. *J. Exp. Biol.* **206**, 4191–4208.

Sane, S. P. & Dickinson, M. H. 2001 The control of flight force by a flapping wing: lift and drag production. *J. Exp. Biol.* **204**, 2607–2626.

Sane, S. P. & Dickinson, M. H. 2002 The aerodynamic effects of wing rotation and a revised quasi-steady model of flapping flight. *J. Exp. Biol.* **205**, 1087–1096.

Smith, M., Wilkin, P. & Williams, M. 1996 The advantages of an unsteady panel method in modeling the aerodynamic forces on rigid flapping wings. *J. Exp. Biol.* **199**, 1073–1083.

Srygley, R. B. & Thomas, A. L. R. 2002 Unconventional lift-generating mechanisms in free-flying butterflies. *Nature* **420**, 660–664.

Sun, M. & Tang, J. 2002 Unsteady aerodynamic force generation by a model fruit fly wing in flapping motion. *J. Exp. Biol.* **205**, 55–70.

Thomas, P. D. & Lombard, C. K. 1979 Geometric conservation law and its application to flow computations on moving grids. *AIAA J.* **17**, 1030–1037.

Wang, Z. J. 2000*a* Two dimensional mechanism for insect hovering. *Phys. Rev. Lett.* **85**, 2216–2219.

Wang, Z. J. 2000*b* Vortex shedding and frequency selection in flapping flight. *J. Fluid Mech.* **410**, 323–341.

Wang, Z. J. 2005 Dissecting insect flight. *Annu. Rev. Fluid. Mech.* **37**, 183–210.

Wang, Z. J., Birch, J. M. & Dickinson, M. H. 2004 Unsteady forces and flows in low Reynolds number hovering flight: two-dimensional computations vs robotic wing experiments. *J. Expl Biol.* **207**, 461–474.

Weis-Fogh, T. 1973 Quick estimates of flight fitness in hovering animals, including novel mechanisms for lift production. *J. Exp. Biol.* **59**, 169–230.

Wu, J. C. 1981 Theory for aerodynamic force and moment in viscous flows. *AIAA J.* **19**, 432–441.